Nucleolar structure connects with global nuclear organization

Chen Wang[1], Hanhui Ma[2,6], Susan J. Baserga[3,4,5], Thoru Pederson[2] and Sui Huang[1*]

[1] Department of Cell and Developmental Biology, Northwestern University Feinberg School of Medicine, Chicago, IL

[2] Department of Biochemistry and Molecular Biotechnology, University of Massachusetts Chan Medical School, Worcester, MA

[3] Department of Genetics, Yale School of Medicine, New Haven, CT

[4] Department of Molecular Biophysics and Biochemistry, Yale University, New Haven, CT

[5] Department of Therapeutic Radiology, Yale School of Medicine, New Haven, CT

[6] School of Life Science and Technology, Shanghai Tech University, Shanghai, China

Running Head: Nucleolar structure impacts nuclear organization

Abbreviations:

PML	promyelocytic leukaemia
BrU	Bromouridine
EM	Electron microscope
CRISPR	Clustered regularly interspaced short palindromic repeats
NOR	Nucleolar organization region
PNC	Perinucleolar compartment

FC	Fibrillar center
DFC	Dense fibrillar components
GC	Granular components

Abstract:

The nucleolus is a multi-functional nuclear body. To tease out the roles of nucleolar structure without resorting to multi-action drugs, we knocked down RNA polymerase I subunit RPA194 in HeLa cells by siRNA. Loss of RPA194 resulted in nucleolar structural segregation and effects on both nucleolus-proximal and distal nuclear components. The perinucleolar compartment was disrupted, centromere-nucleolus interactions were significantly reduced, and the intranuclear locations of specific genomic loci were altered. Moreover, Cajal bodies, distal from nucleoli, underwent morphological and compositional changes. To distinguish whether these global reorganizations are the results of nucleolar structural disruption or inhibition of ribosome synthesis, the pre-ribosomal RNA processing factor, UTP4, was also knocked down, which did not lead to nucleolar segregation, nor the intranuclear effects seen with RPA195A knockdown, demonstrating that they do not arise from a cessation of ribosome synthesis. These findings point to a commutative system that links nucleolar structure to the maintenance and spatial organization of certain nuclear bodies and genomic loci.

Introduction

The nucleus is highly compartmentalized, with interphase chromosomes organized into specific territories and interchromatin space occupied by various non-membrane enclosed organelles, such as Cajal and PML bodies, and interchromatin granule clusters (Misteli and Spector, 2011; Pederson, 2011). The nucleolus is the most prominent nuclear body and is the site of ribosome synthesis as well as other functions that have since come into view, including assembly of the signal recognition particle, cell cycle progression, macromolecular trafficking, and surveillance of genotoxic and nucleolar stress (Baserga and DiMario, 2018; Baserga et al., 2020; Lin et al., 2014; Nemeth and Grummt, 2018; Pederson, 2011; Pederson and Tsai, 2009). Here we have deployed a new strategy to explore whether the nucleolar structure might have a additional role in the cell that are independent from ribosome synthesis.

A frequently deployed tool for investigating the nucleolus has been exposure of cells to a low concentration of actinomycin D. A pioneering study that correlated a reduction of ^{3}H-uridine labeling of the nucleolus with a biochemical demonstration of impaired ribosomes synthesis

(Perry, 1962) was one of the key steps in defining the nucleolus as the site of ribosome biogenesis. It was subsequently found that exposure of mammalian cells to low concentrations of actinomycin D also leads to alterations of nucleolar morphology, in which its three ultrastructurally-defined components, fibrillar center (FC), dense fibrillar components (DFC) and granular components (GC), undergo repositioning, (Clark et al., 1967). At these low concentrations, actinomycin D preferentially intercalates and alkylates DNA at adjacent GC base pairs (Gallego et al., 1997; Sengupta et al., 1988). Since ribosomal RNA genes of eukaryotic cells are GC- rich (at least 65-70% in the case of most mammalian genomes), there has been a tendency to regard low actinomycin as a highly specific experimental intervention. However, there are numerous other GC-rich sites throughout mammalian genomes. Indeed, our bioinformatics survey of the human reference genome revealed 320 sites which are 65-70% GC, including some that are 85% or more (Table S1). Thus, it is possible that nucleolar disruption by actinomycin D and concurrently observed effects could be attributable to the drug's action at one or more of these hundreds of genomic sites or to other yet to be defined actions of the drug.

The circumvent the pitfalls of using small molecule drugs with multi-valent functions, we employed siRNA approach to disrupt rDNA transcription machinery to determine whether the loss of transcription machinery impacts the well-defined nucleolar structure as actinomycin D treatment does. We also address whether nucleolar structure maintenance is dependent upon ribosome synthesis and whether nucleolar structural integrity plays a role in the organization of other nuclear domains.

Results

Knockdown of RPA194 phenocopies low actinomycin D treatment

We used siRNA knockdown of RPA194, the largest subunit of RNA polymerase I (Russell and Zomerdijk, 2005), to disrupt rDNA transcription. Seventy-two hours after transfection, the level of RPA194 was reduced by more than 95% while the levels of another rDNA transcription factor, UBF, remain unchanged (Fig. 1A). Knockdown of RPA194 led to an inhibition of rRNA synthesis as measured both by pulse-labeling cells with BrU and qRT-PCR of the 5′ ETS regions of the nascent pre-rRNA (Suppl. Fig. 1A and 1B). As expected, there was a resultant reduction of ribosome synthesis as assessed by tracking an inducible GFP-tagged ribosomal protein RPL29 (Wild et al., 2010) (Fig. 1B). In untreated and control siRNA transfected cells, GFP-RPL29 was localized in both nucleoli and the cytoplasm within 24 hours of activation, reflecting its assembly into new ribosomes and localization to the cytoplasm. In comparison, in RPA194 knockdown cells, GFP-RPL29 was detected only in nucleoli and not in the cytoplasm 24 hours after activation, indicating the lack of newly synthesized ribosomal particles bearing GFP tagged RPL29 entering the cytoplasm. When the pre-ribosomal RNA processing factor UTP4 (Freed et al., 2012) was knocked down, ribosome synthesis was similarly blocked (Fig. 1B), as also represented by a similar lack of cytoplasmic GFP-RPL29 signal. These results demonstrate the inhibition of ribosome synthesis by knockdown of either RPA194 or UTP4.

Electron microscopy (EM) revealed that knockdown of RPA194 resulted in a reorganization of nucleolar architecture. The nucleolus normally contains three distinct ultrastructural components: FC (Fig. 2A, arrows), DFC (Fig. 2A, arrowheads) and GC (Fig. 2A, asterisk) (Pederson, 2011; Raska, 2003). Knockdown of RPA194 induced segregation of the fibrillar components from the granular components (Fig. 2A, left panel). The nucleolar segregation observed by EM corresponds to the redistribution of the fibrillar protein, UBF (Fig. 2B, arrowheads) and the dense fibrillar component marker protein fibrillarin (Suppl. Fig. 2) from their normal nucleolar location into nucleolar caps (Fig. 2B, arrows). Quantitative analyses revealed that the loss of RPA194 in siRNA treated cells closely paralleled nucleolar segregation (Fig. 2C), similar to that observed in cells treated with low concentrations of actinomycin D (Suppl. Fig. 3). In comparison to the knockdown of RPA194, siUTP4 treatment, while also blocking ribosome synthesis, did not lead to nucleolar segregation (Fig. 1B, 2A, B and C). This demonstrated, for the first time, that nucleolar segregation is not the result of ribosome synthesis inhibition, but rather the disruption of rDNA transcription machinery.

The spatial redistribution of the fibrillar centers upon nucleolar segregation implies that the rDNA does so in parallel. To determine if this was the case, we deployed CRISPR-dCas9 mediated labeling of rDNA clusters in siRNA treated and control cells (Ma et al., 2015; Ma et al., 2019; Ma et al., 2018; Ma et al., 2016a; Ma et al., 2016b). Sixteen sets of CRISPR-Cas9 gs RNA were designed to label rDNA. The specificity of the labeling was validated by simultaneous labeling with an anti-UBF antibody on mitotic Nucleolar Organizer Regions (NORs) (Suppl. Fig. 4) as it has been shown that rDNA transcription factors remain bound to active NORs throughout mitosis (Roussel et al., 1996). In untreated cells, control siRNA or siUTP4 transfected cells, the labeled rDNA was localized in the nucleoli in the expected nucleolar pattern. But after RPA194 knockdown, the rDNA signals became redistributed and colocalized with the repositioned fibrillarin caps (Fig. 3A and C). This was also the case with low actinomycin treatment (Fig. 3B and C), consistent with findings from a recent study (Mangan and McStay, 2021). In both cases, nearly all the rDNA was associated with the fibrillar protein-localized caps (Fig. 3A, B, and C). These findings together with those in Fig. 1 show that RPA194 knockdown recapitulates in the classical phenomenon of nucleolar segregation observed with the treatment of low actinomycin.

Nucleolus-proximal nuclear domains are altered by knockdown of RPA194, but not UTP4.

With siRPA194 knockdown as a selective tool to disrupt nucleolar structure without the drawbacks of drug treatment, we asked whether nucleolar structure might play a role in nuclear organization. The perinucleolar compartment (PNC) is a distinct structure in many cancer cell types, including HeLa cells, and is physically associated with the nucleolus (Norton et al., 2008; Pollock and Huang, 2009). In a previous study, knockdown of RPA194 resulted in disassembly of PNCs (Frankowski et al., 2018). To investigate whether PNC disruption is the consequence of ribosome synthesis or rather due to nucleolar structure alteration, we included siUTP4 knockdown as a control. Antibodies against PTB (polypyrimidine binding protein, a fiduciary marker protein of the PNC) were used to immunolabel PNCs. As shown in Fig. 4A and B, while the siRPA194 treatment reduced PNC prevalence, knockdown of UTP4 did not significantly impact PNC bodies. Additionally, most of the remaining PNCs underwent structural alteration, becoming crescent moon shaped (Fig. 4A, arrows) in siRPA194 treated cells. Thus, PNC integrity is dependent on the nucleolar structure or rDNA transcription machinery, rather than ribosome synthesis.

Centromeres are known to cluster around nucleoli (Padeken and Heun, 2013), with an average 60% of the centromeres situated close to nucleoli in the HeLa cells we have used here (Foltz et al., 2009). To evaluate whether nucleolar segregation impacts nucleolus-centromere proximity, we immunolabeled centromeres (of all chromosomes) and nucleoli with anti-CENPA and anti-UBF antibodies respectively. As shown in Figure 5A and B, upon RPA194 knockdown centromeres were less frequently associated with nucleoli and more dispersed throughout the nucleus. In contrast, UTP4 knockdown did not change nucleolus-centromere associations (Fig. 5A and B). These findings indicate that the nucleolus- proximal centromere arrangement is contingent on normal nucleolar organization or Pol I transcription.

Repositioning of genomic loci after RPA194 knockdown

We next asked whether there are more wide-ranging effects throughout the 3-D nucleome upon RPA194 knockdown and the resulting nucleolar reorganization. As shown in Fig. 6A, the HIST1H2BN locus underwent a repositioning from its mainly nucleolar proximity to a predominantly central nuclear location in siRPA194 treated cells. Conversely, the predominantly central MALL locus become repositioned to more nuclear-peripheral positions (Fig. 6B). These positional changes of genomic loci were not observed in either siUTP4 or control oligo treated cells, nor in untreated cells, and thus are specifically attributable to RPA194 knockdown coupled nucleolar segregation.

Nucleolar organization governs Cajal body integrity

Given these results, we wondered if normal nucleolar organization might play a role not only in the intranuclear spatial location of certain genomic loci, but perhaps also in the maintenance of nuclear bodies. We therefore examined Cajal bodies (Gall, 2003; Nizami et al., 2010; Verheggen et al., 2002; Wang et al., 2016) and found that RPA194 knockdown, but not siUTP4 knockdown, led to their disruption as tracked both by the localization of p80 coilin, a Cajal body marker, and fibrillarin or UBF (Fig. 7A, and Suppl. Fig. 5). The disruption of Cajal bodies was closely correlated with nucleolar segregation (Fig. 7B) like those previously described in actinomycin D-treated cells (Shav-Tal et al., 2005). The dispersion of Cajal bodies was also observed when examined with the additional marker protein SMN (Fig. 8). In addition to the dramatic structural changes, the Cajal body proteins, SMN and coilin no longer perfectly colocalized as shown in Fig. 8. These findings demonstrate that the nucleolus, in its normal operation, not only impacts genomic organization, but also a class of nuclear bodies usually situated distant from it.

The observed disruption of Cajal bodies prompted us to ask if RPA194 knockdown influences another nuclear body, the histone locus body (Nizami et al., 2010). As shown in Suppl. Fig. 6, there was no effect of RPA194 knockdown on histone locus bodies, demonstrating that not all nuclear bodies are regulated by an intact nucleolar structure.

Discussion

To circumvent the lack of specificity of low actinomycin D treatment as a tool to investigate the possible roles of nucleolar structure in global nuclear organization, we deployed knockdown of the Pol I subunit, RPA194, and of the pre-rRNA processing factor, UTP4, both leading to ribosome synthesis inhibition. However, only siRPA194 knockdown, but not UTP4 knockdown, induced nucleolar segregation, indicating that continuous ribosome synthesis is not required for maintenance of the classical tripartite nucleolar ultrastructure and gave us an opportunity to specifically address the impact of nucleolar structure on other nuclear components. We chose to use HeLa cells because they lack the p53 protein, which might otherwise trigger apoptosis upon RPA194 knockdown. We found that nucleolar segregation leads to changes throughout the 3D nucleome, in which nucleolus-proximal entities such as the PNC and centromere clusters reorganize significantly, certain genomic loci change their spatial distribution from nucleolus-proximal to central nuclear locations or from mostly nuclear central to the nuclear periphery. In addition, nucleolar segregation disrupts nucleoplasmic Cajal bodies, but not histone locus bodies.

Our findings demonstrate a connection between nucleolar structure and a subset of various intranuclear components or genomic loci, with no apparent connection with others. The nature of the underlying signaling network is not clear. One possibility is that nucleolar segregation alters physical contacts between the nucleolar surface and directly connecting elements, such as nucleolus-proximal heterochromatin (Vertii et al., 2019), other nucleolus-associated domains of the genome (Nemeth et al., 2010; van Koningsbruggen et al., 2010), PNCs, or clustered centromeres. There is, moreover, extensive evidence for shuttling of proteins between the nucleolus and the nucleoplasm both in normal circumstances (Chen and Huang, 2001; Phair and Misteli, 2000) and in actinomycin D-induced nucleolar segregation (Shav-Tal et al., 2005). Thus, it is also possible that nucleolar segregation restricts the dynamics and exchanges of nucleolar and nuclear components that are part of the regulatory network important to nuclear homeostasis. Future studies will investigate the mechanics and mechanisms of these connections.

Material and Methods:

Cell culture. HeLa cells were maintained in DMEM (ThermoFisher Scientific) with 10% FBS (GEMINI Bio Products) and 100 units/ml of penicillin and streptomycin (ThermoFisher Scientific). RPL29-GFP cells were cultured in DMEM with 0.3mg/ml of hygromycin and 0.5ug/ml puromycin. Cells were generally plated 24 h prior to treatment with siRNA.

RNA interference. The siRNA targeting human RPA194 was obtained from Invitrogen (cat#: 10620318) as was a negative control siRNA (cat#: 12935-300). The siRNA targeting human UTP4 was obtained from GE Dharmacon (cat#: M-015011-01-0005). siRNA were transfected into cells with Lipofectamine® RNAiMAX Transfection Reagent (Thermofisher Scientific; cat#: 13778) according to manufacturer's instructions. The reported experiments were performed after 72 hours transfection.

Immunofluorescence: Primary antibodies were from the indicated sources and used at the stated dilutions: RPA194, Santa Cruz Biotechnology, cat #sc-48385, 1:100; PTB (S. Huang laboratory), 1:300; UBF, Santa Cruz Biotechnology, cat#: sc-13125, 1:50; fibrillarin, Sigma, cat #: ANA-N, 1:10; CENPA (Thermo Fisher #MA1-20832, 1:100; coilin, Santa Cruz Biotechnology, cat#: sc-32860, 1:300; Flash histone locus antibody protein (Gall lab), 1:500; SMN, Santa Cruz Biotechnology, cat.# sc-15320, 1:300. The fluorescein conjugated (Jackson ImmunoResearch) and Alexa Fluor-labeled (ThermoFisher) secondary antibodies were used at a dilution of 1:200. Slides were visualized on a Nikon Eclipse Ti-E inverted fluorescence microscope using NIS-Elements AR 4.2 software (Nikon).

Western blots. These were performed according to manufacture protocols (Millipore). The primary antibodies and dilutions used were RPA194 (see above), 1:500); UBF (see above), 1:500); beta-actin (Sigma, cat.# A5060), 1:3000, as loading controls. LI-COR IRDye secondary antibodies (1:10,000) were used for visualization. Protein bands were detected using LI-COR Odyssey Image Studio (LI-COR Biosciences).

Electron microscopy. Cells were in fixed 2% paraformaldehyde-2.5% glutaraldehyde in 0.1M cacodylate buffer, pH 7.3, processed and examined in the Northwestern University Feinberg School of Medicine Imaging Facility.

Inducible expression of RPL29-GFP HeLa cell line. The tetracycline-inducible RPL29-GFP cell line was maintained in hygromycin and puromycin. Before each experiment the cells were transferred to medium without the antibiotics and transfected with the desired siRNA or left untreated. After 48 hours, tetracycline was added at 125 ng/ml to induce RPL29-GFP expression followed by examination 20 hours later.

In situ hybridization. HeLa cells were seeded to 6 well plates one day before transfection of siRNAs. Three days post-transfection, the genomic loci HIST1H2BN and MALL were detected using BACs obtained from bac.chori.org (cat. #'s RP-11-958P15 and RP11-349F11, respectively, and labeled by nick translation Abbott Laboratories (cat. # 07J00-001. The hybridization signals were measured using the Z series photos taken on a Nikon Eclipse Ti-E inverted fluorescence microscope. The gene loci spatial positions were analyzed in their relation to the nuclear envelope and nucleoli, and the space between.

CRISPR dCas9 labeling of rDNA. The CRISPR Cas9 rDNA labeling constructs were "Nm dCas9 3XGFP" as detailed in (Ma et al., 2015) and a U6 promoter guide RNA plasmid containing a pool of 16 fragments complementary to rDNA. The sequences are detailed here. rDNA-F1: ACCGCGCGTGTTCTCATCTAGAAG; rDNA-R1: AAACCTTCTAGATGAGAACACGCG; rDNA-F2: ACCGTGGGCAGAACGAGGGGGACC; rDNA-R2: AAACGGTCCCCCTCGTTCTGCCCA; rDNA-F3: ACCGCGGACACAGCACTGACTACC; rDNA-R3: AAACGGTAGTCAGTGCTGTGTCCG; rDNA-F4: ACCGCCACCTCCTTGACCTGAGTC; rDNA-R4: AAACGACTCAGGTCAAGGAGGTGG; rDNA-F5: ACCGTCGCTCTGTCACCCAGGCTG; rDNA-R5: AAACCAGCCTGGGTGACAGAGCGA; rDNA-F6: ACCGTCTTCGGTAGCTGGGATTAC; rDNA-R6: AAACGTAATCCCAGCTACCGAAGA; rDNA-F7: ACCGTCCTGGGCCTCCCAAAGTGC; rDNA-R7: AAACGCACTTTGGGAGGCCCAGGA; rDNA-F8: ACCGTAGGCCATTGCACTGTAGCC; rDNA-R8: AAACGGCTACAGTGCAATGGCCTA; rDNA-F9: ACCGACGTCTGTCATCCCGAGGTC; rDNA-R9: AAACGACCTCGGGATGACAGACGT; rDNA-F10: ACCGCGAAATGGAGTCAGGCGCCG; rDNA-R10:

AAACCGGCGCCTGACTCCATTTCG; rDNA-F11: ACCGTGTAACCCCAGCTACTCGGG; rDNA-R11: AAACCCCGAGTAGCTGGGGTTACA; rDNA-F12: ACCGAATTGCTTGAACCTGGCAGG; rDNA-R12: AAACCCTGCCAGGTTCAAGCAATT; rDNA-F13: ACCGCTGGGCGACAGAGTGAGACC; rDNA-R13: AAACGGTCTCACTCTGTCGCCCAG; rDNA-F14: ACCGACTGTATTGCTACTGGGCTA; rDNA-R14: AAACTAGCCCAGTAGCAATACAGT; rDNA-F15: ACCGCCGAGAGGAATCTAGACAGG; rDNA-R15: AAACCCTGTCTAGATTCCTCTCGG; rDNA-F16: ACCGGGTCCCCGCTTGGATGCGAG; rDNA-R16: AAACCTCGCATCCAAGCGGGGACC. HeLa cells were seeded onto 6 well plates. siRNAs were transfected as described above a day after seeding. After another 24 hours, the dCas9 and gsRNAs were transfected to corresponding wells with Lipofectamine 2000 according to manufacturer's instruction at a concentration of 200 ng of dCas9 and 750 ng sgRNA individually. Signals were evaluated 42 hours post-transfection using Nickon fluorescence microscope. Actinomycin D was applied at a concentration of 0.04 ug/ml for 3 hours at 42 hours post-CRISPR construct transfection.

Supplemental materials: They include additional supporting data including 1 table and figures.

Acknowledgements

This study was funded by NIH grants 2 R01 GM078555-09 and U01CA260699 to S.H., 1R35GM131687 to S.J.B and U01 DA-040588 to T.P. and Paul Kaufman, UMass Chan Medical School, the latter part of the NIH 4-D Nucleome Initiative. We thank Lihua Julie Zhu and Paul Kaufman at UMass Chan Medical School for expertise on the bioinformatics search of GC-rich loci in the human genome. We also thank Dr. Samuel Sondalle for part of protein expression analyses. In addition, we thank Ulrike Kutay (Institute of Biochemistry, ETH Zurich, Zurich, Switzerland) for the GFP-RPL29 construct, Zehra Nizami and Joseph Gall (Department of Embryology, Carnegie Institution for Science) for the anti-FLASH antibody. We would like to thank Tom Volpe, Northwestern U. for critical reading of the manuscript.

Author contributions: S.H. designed the project; H.M. and T.P. provided the CRISPR-dCas9 rDNA labeling system; C.W.; S.J.B. provided the UTP4 siRNA knockdown plasmid and

contributed to the manuscript preparation; S.H. and T.P. wrote the paper with input from all authors.

References:

Baserga, S.J., and P.J. DiMario. 2018. Emerging roles for the nucleolus 2017. *Mol Biol Cell*. 29:773-775.

Baserga, S.J., P.J. DiMario, and F.E. Duncan. 2020. Emerging roles for the nucleolus 2019. *J Biol Chem*. 295:5535-5537.

Chen, D., and S. Huang. 2001. Nucleolar components involved in ribosome biogenesis cycle between the nucleolus and nucleoplasm in interphase cells. *J Cell Biol*. 153:169-176.

Clark, A.M., R. Love, G.P. Studzinski, and K.A. Ellem. 1967. A correlated morphological and functional study of the effects of actinomycin D on HeLa cells. I. Effects on the nucleolar and cytoplasmic ribonucleoproteins. *Exp Cell Res*. 45:106-119.

Foltz, D.R., L.E. Jansen, A.O. Bailey, J.R. Yates, 3rd, E.A. Bassett, S. Wood, B.E. Black, and D.W. Cleveland. 2009. Centromere-specific assembly of CENP-a nucleosomes is mediated by HJURP. *Cell*. 137:472-484.

Frankowski, K.J., C. Wang, S. Patnaik, F.J. Schoenen, N. Southall, D. Li, Y. Teper, W. Sun, I. Kandela, D. Hu, C. Dextras, Z. Knotts, Y. Bian, J. Norton, S. Titus, M.A. Lewandowska, Y. Wen, K.I. Farley, L.M. Griner, J. Sultan, Z. Meng, M. Zhou, T. Vilimas, A.S. Powers, S. Kozlov, K. Nagashima, H.S. Quadri, M. Fang, C. Long, O. Khanolkar, W. Chen, J. Kang, H. Huang, E. Chow, E. Goldberg, C. Feldman, R. Xi, H.R. Kim, G. Sahagian, S.J. Baserga, A. Mazar, M. Ferrer, W. Zheng, A. Shilatifard, J. Aube, U. Rudloff, J.J. Marugan, and S. Huang. 2018. Metarrestin, a perinucleolar compartment inhibitor, effectively suppresses metastasis. *Sci Transl Med*. 10.

Freed, E.F., J.L. Prieto, K.L. McCann, B. McStay, and S.J. Baserga. 2012. NOL11, implicated in the pathogenesis of North American Indian childhood cirrhosis, is required for pre-rRNA transcription and processing. *PLoS Genet*. 8:e1002892.

Gall, J.G. 2003. The centennial of the Cajal body. *Nat Rev Mol Cell Biol*. 4:975-980.

Gallego, J., A.R. Ortiz, B. de Pascual-Teresa, and F. Gago. 1997. Structure-affinity relationships for the binding of actinomycin D to DNA. *J Comput Aided Mol Des*. 11:114-128.

Lin, T., L. Meng, T.C. Lin, L.J. Wu, T. Pederson, and R.Y. Tsai. 2014. Nucleostemin and GNL3L exercise distinct functions in genome protection and ribosome synthesis, respectively. *J Cell Sci*. 127:2302-2312.

Ma, H., A. Naseri, P. Reyes-Gutierrez, S.A. Wolfe, S. Zhang, and T. Pederson. 2015. Multicolor CRISPR labeling of chromosomal loci in human cells. *Proc Natl Acad Sci U S A*. 112:3002-3007.

Ma, H., L.C. Tu, Y.C. Chung, A. Naseri, D. Grunwald, S. Zhang, and T. Pederson. 2019. Cell cycle- and genomic distance-dependent dynamics of a discrete chromosomal region. *J Cell Biol*. 218:1467-1477.

Ma, H., L.C. Tu, A. Naseri, Y.C. Chung, D. Grunwald, S. Zhang, and T. Pederson. 2018. CRISPR-Sirius: RNA scaffolds for signal amplification in genome imaging. *Nat Methods*. 15:928-931.

Ma, H., L.C. Tu, A. Naseri, M. Huisman, S. Zhang, D. Grunwald, and T. Pederson. 2016a. CRISPR-Cas9 nuclear dynamics and target recognition in living cells. *J Cell Biol*. 214:529-537.

Ma, H., L.C. Tu, A. Naseri, M. Huisman, S. Zhang, D. Grunwald, and T. Pederson. 2016b. Multiplexed labeling of genomic loci with dCas9 and engineered sgRNAs using CRISPRainbow. *Nat Biotechnol*. 34:528-530.

Mangan, H., and B. McStay. 2021. Human nucleoli comprise multiple constrained territories, tethered to individual chromosomes. *Genes Dev*. 35:483-488.

Misteli, T., and D.L. Spector. 2011. The Nucleus. *Cold Spring Harbor Laboratory Press*

Nemeth, A., A. Conesa, J. Santoyo-Lopez, I. Medina, D. Montaner, B. Peterfia, I. Solovei, T. Cremer, J. Dopazo, and G. Langst. 2010. Initial genomics of the human nucleolus. *PLoS Genet*. 6:e1000889.

Nemeth, A., and I. Grummt. 2018. Dynamic regulation of nucleolar architecture. *Curr Opin Cell Biol*. 52:105-111.

Nizami, Z., S. Deryusheva, and J.G. Gall. 2010. The Cajal body and histone locus body. *Cold Spring Harb Perspect Biol*. 2:a000653.

Norton, J.T., C.B. Pollock, C. Wang, J.C. Schink, J.J. Kim, and S. Huang. 2008. Perinucleolar compartment prevalence is a phenotypic pancancer marker of malignancy. *Cancer*. 113:861-869.

Padeken, J., and P. Heun. 2013. Centromeres in nuclear architecture. *Cell Cycle*. 12:3455-3456.

Pederson, T. 2011. The nucleolus. *Cold Spring Harb Perspect Biol*. 3:209-223.

Pederson, T., and R.Y. Tsai. 2009. In search of nonribosomal nucleolar protein function and regulation. *J Cell Biol*. 184:771-776.

Perry, R.P. 1962. The Cellular Sites of Synthesis of Ribosomal and 4s RNA. *Proc Natl Acad Sci U S A*. 48:2179-2186.

Phair, R.D., and T. Misteli. 2000. High mobility of proteins in the mammalian cell nucleus. *Nature*. 404:604-609.

Pollock, C., and S. Huang. 2009. The perinucleolar compartment. *J Cell Biochem*. 107:189-193.

Raska, I. 2003. Oldies but goldies: searching for Christmas trees within the nucleolar architecture. *Trends Cell Biol*. 13:517-525.

Roussel, P., C. Andre, L. Comai, and D. Hernandez-Verdun. 1996. The rDNA transcription machinery is assembled during mitosis in active NORs. *J. Cell Biol.* 133:235-246.

Russell, J., and J.C. Zomerdijk. 2005. RNA-polymerase-I-directed rDNA transcription, life and works. *Trends Biochem Sci*. 30:87-96.

Sengupta, S.K., D.P. Rosenbaum, R.K. Sehgal, B. Almassian, and J. Blondin. 1988. Enantiomers of 7-(2,3-epoxypropoxy)actinomycin D as dual-action DNA-acting antitumor agents. *J Med Chem*. 31:1540-1547.

Shav-Tal, Y., J. Blechman, X. Darzacq, C. Montagna, B.T. Dye, J.G. Patton, R.H. Singer, and D. Zipori. 2005. Dynamic sorting of nuclear components into distinct nucleolar caps during transcriptional inhibition. *Mol Biol Cell*. 16:2395-2413.

van Koningsbruggen, S., M. Gierlinski, P. Schofield, D. Martin, G.J. Barton, Y. Ariyurek, J.T. den Dunnen, and A.I. Lamond. 2010. High-resolution whole-genome sequencing reveals that specific chromatin domains from most human chromosomes associate with nucleoli. *Mol Biol Cell*. 21:3735-3748.

Verheggen, C., D.L. Lafontaine, D. Samarsky, J. Mouaikel, J.M. Blanchard, R. Bordonné, and E. Bertrand. 2002. Mammalian and yeast U3 snoRNPs are matured in specific and related nuclear compartments. *EMBO J*. 21:2736-2745.

Vertii, A., J. Ou, J. Yu, A. Yan, H. Pages, H. Liu, L.J. Zhu, and P.D. Kaufman. 2019. Two contrasting classes of nucleolus-associated domains in mouse fibroblast heterochromatin. *Genome Res*. 29:1235-1249.

Wang, Q., I.A. Sawyer, M.H. Sung, D. Sturgill, S.P. Shevtsov, G. Pegoraro, O. Hakim, S. Baek, G.L. Hager, and M. Dundr. 2016. Cajal bodies are linked to genome conformation. *Nat Commun*. 7:10966.

Wild, T., P. Horvath, E. Wyler, B. Widmann, L. Badertscher, I. Zemp, K. Kozak, G. Csucs, E. Lund, and U. Kutay. 2010. A protein inventory of human ribosome biogenesis reveals an essential function of exportin 5 in 60S subunit export. *PLoS Biol*. 8:e1000522.

Figure Legends

Figure 1: siRPA194 and siUTP treatment in HeLa cells significantly reduced ribosome synthesis, but only siRPA194 treatment induces nucleolar segregation. (A) The level of RPA194 protein was significantly reduced while the UBF level was unchanged at 72 hours after transfection. (B) Both siRPA194 and siUTP4 treatment inhibited ribosome synthesis as assayed in an inducible GFP-RPL29 stably transfected HeLa cell line. Activation of fusion protein expression 48 hours after transfection showed little presence of GFP-RPL29 in the cytoplasm in siRPA194 and siUTP4 compared to control cells, demonstrating lack of new ribosome synthesis. Bars = 5 mm

Figure 2: siRPA194 knockdown cells induced nucleolar segregation. (A) Examination by electron microscopy demonstrated the siRPA194 treatment (left panel) in HeLa cells changed nucleolar structures where the fibrillar components (arrows) were segregated from the granular components (*). In comparison, the nucleolus in UTP4 knockdown cells (middle panel) maintained the typical three structural components, fibrillar center (arrow), dense fibrillar components (arrowhead), and granular components (*) as those in the siControl or untreated cells (right panels). (B) Correspondingly, siRPA194 treated, but not siUTP4 treated or control cells, showed segregated caps like localization of UBF as detected at the immunofluorescence microscope level. (C) Quantification showed that the segregation of nucleoli occurs mostly in RPA194 knockdown HeLa cells (n>100 cells, $p<0.005$ between siRPA194 and all other conditions). Bars =5 mm.

Figure 3: rDNA co-segregated with the fibrillar proteins (fibrillarin or UBF) present in cap structures in segregated nucleoli. (A) Eleven sets of CRISPR-Cas9 sgRNA specifically complementing the rDNA were labeled with MS2-GFP, showing the localization of the rDNA chromatin, which redistributed with the fibrillar components to the nucleolar caps in siRPA194 treated HeLa cells (arrows) similarly to (B) those treated by ActD (arrows). (C) Quantitative evaluation indicated the co-partitioning of rDNA chromatin with the fibrillar components in nearly all of cells treated by siRPA194 or ActD (n>100 cells). Bars = 5 mm

Figure 4: PNC structure and prevalence were altered in siRPA194, but not in siUTP4 treated HeLa cells. (A) The shape of most PNCs was changed, becoming extended (arrows) in siRPA194 treated, but not in siUTP4 treated or control cells. (B) Quantitative analyses demonstrated a significant reduction of PNC prevalence in siRPA194 treated cells (n>100 cells). Bars = 5 mm ****p<0.001

Figure 5: RPA194 knockdown changed nucleoli-centromere interactions (A) The clustering of centromeres (green) around nucleoli (red) decreased in siRPA194 treated, but not in siUTP4 treated and control cells. (B) Quantifying analyses showed changes were statistically significant (n>50 cells) ****p<0,001. Bars = 5 mm

Figure 6: RPA194 knockdown changed spatial distributions of some genes. (A) HIST1H2BN gene loci became more centrally localized in siRPA194 treated HeLa cell nuclei than siUTP4 treated and other control cells (arrowheads) whereas (B) MALL loci became more nuclear peripherally localized in siRPA194 treated cells (arrowheads). Corresponding quantitative analyses showed significant differences in central and peripheral localization of the gene loci between treated and control cells. (n>50 cells) p<0.01. Bars = 5 mm

Figure 7: siRPA194, but not siUTP4 treatment, induced disruption of Cajal bodies (arrows). (A) Upon siRPA194 treatment, Cajal bodies became irregularly shaped and some juxtaposed segregated nucleoli in siRPA194 treated cells (third panels), as detected using anti-coilin antibodies. However, Cajal bodies remained round-punctuated spots (arrows) in siUTP4 or control treated cells. (B) Quantitative evaluation showed a close coupling between nucleolar segregation and disruption of Cajal bodies (n>100 cells) (p<0.001 between siRPA194 and all others).

Figure 8: Cajal body components no longer showed nearly complete colocalization in cells with segregated nucleoli from the treatment of siRPA194. Each panel shows a single nucleus. SMN and coilin which normally colocalize to the dotted-like Cajal body structures (Merge) no longer perfectly coincide in the round spots, rather become less colocalized in siRPA194 treated cells (arrowhead). Bar= 5mm

Supplemental material:

Suppl. Table 1: * The exonic and intronic regions of the human reference genome hgp38 were searched with a criterion set at a GC content of between 65 and 100%, as detailed in Materials and Methods. NA: not annotated.

Suppl. Figure 1: The transcription of rDNA was significantly reduced in cells treated with siRPA194 and to a lesser extent with siUTP4. (A) BrU pulse labeling for 5 minutes showed a significant loss of BrU signal in siRPA194 treated cells (A, arrows), compared to controls where more intense labeling was detected in nucleoli. (B) Quantitative RT-PCR showed a significant reduction in 5'ETS RNA expression in siRPA194 and siUTP4 treated cells. Bar= 5 mm. ****$p<0.001$, **$p<0.01$

Suppl. Figure 2: siRPA194, but not siUTP4 treated HeLa cells, lost the RPA194 signal (green). Nucleolar segregation was detected by the immunolabeling of fibrillarin (magenta). Cap-like structures enriched with firbrillar components (arrows) juxtaposed the reminants of the nucleoli primarily containing granular components (arrowheads). Bars= 5 mm

Suppl. Figure 3: Treatment with a low concentration (0.04ug/ml) of actinomycin D (Act D) induces nucleolar segregations and disruption of Cajal bodies as detected by anti-fibrillarin antibodies (red) and anti-coilin (green) antibodies. Bar= 5 mm

Suppl. Figure 4: The CRISPR-Cas9 sgRNA labeling of rDNA was validated using mitotic cells where UBF was found to be colocalized with the labeling (arrows), confirming that the sgRNA sets indeed labeled rDNA chromatin on mitotic chromosomes (arrow). Bar= 5 mm

Suppl. Fig. 5: Cajal bodies are significantly altered in siRPA194 treated cells. Cells were co-immunolabeled with antibodies against UBF and coilin. Bar= 5 mm

Suppl. Figure 6: While Cajal bodies change significantly in siRPA194 treated cells, histone locus bodies do not show detectable changes. Bar= 5 mm

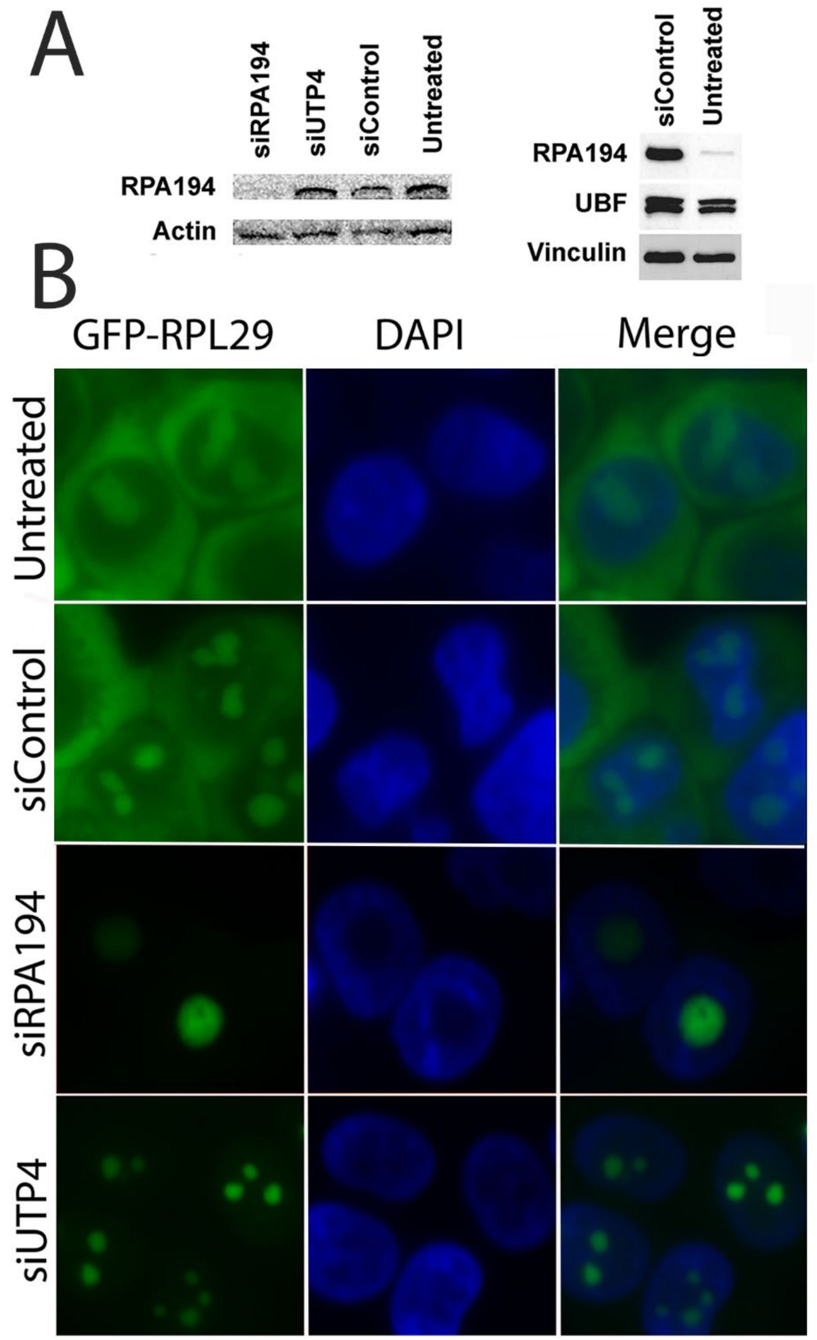

Figure 1: siRPA194 and siUTP treatment in HeLa cells significantly reduced ribosome synthesis, but only siRPA194 treatment induces nucleolar segregation. (A) The level of RPA194 protein was significantly reduced while the UBF level was unchanged at 72 hours after transfection. (B) Both siRPA194 and siUTP4 treatment inhibited ribosome synthesis as assayed in an inducible GFP-RPL29 stably transfected HeLa cell line. Activation of fusion protein expression 48 hours after transfection showed little presence of GFP-RPL29 in the cytoplasm in siRPA194 and siUTP4 compared to control cells, demonstrating lack of new ribosome synthesis. Bars = 5 μm

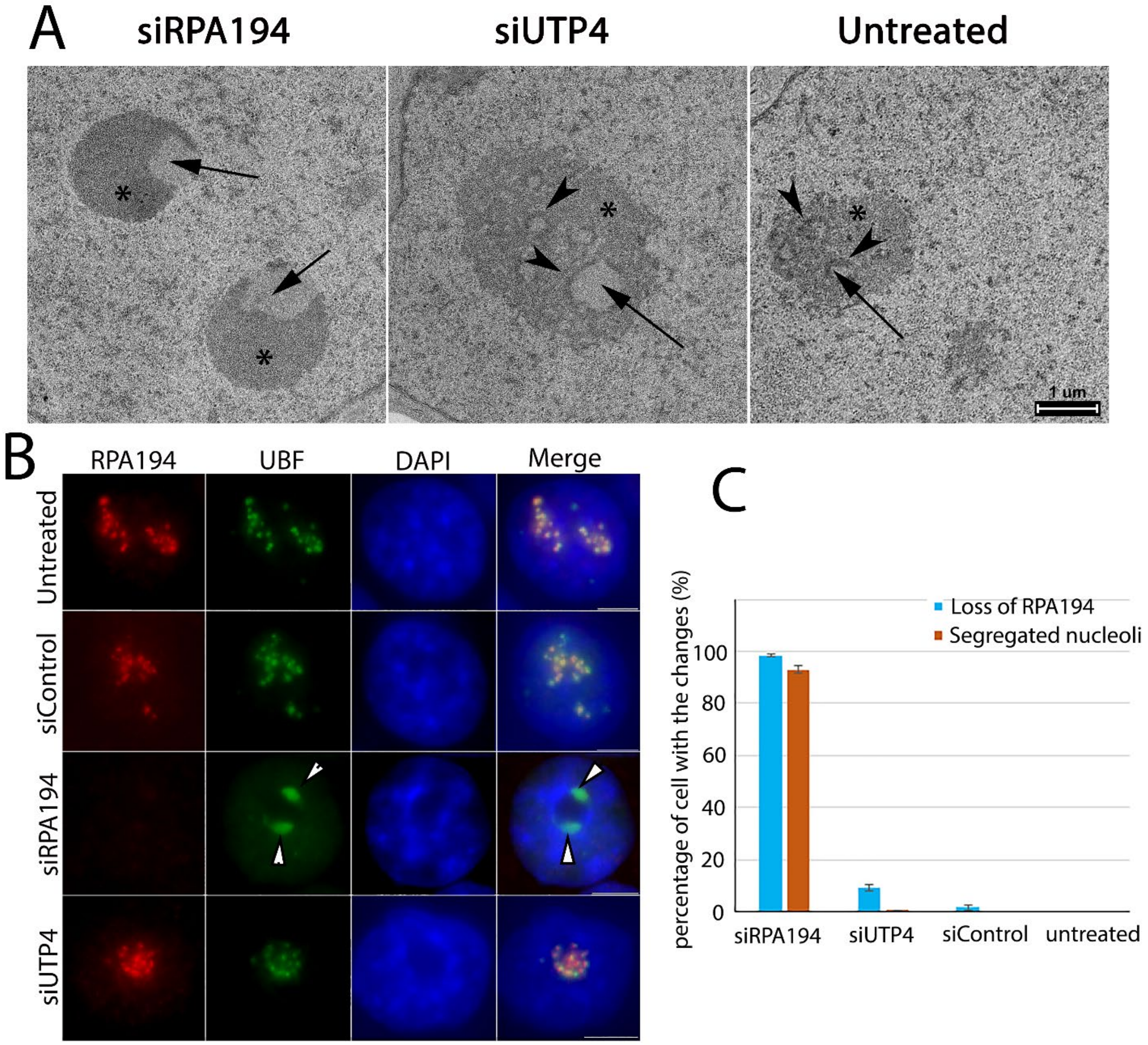

Figure 2: siRPA194 knockdown cells induced nucleolar segregation. (A) Examination by electron microscopy demonstrated the siRPA194 treatment (left panel) in HeLa cells changed nucleolar structures where the fibrillar components (arrows) were segregated from the granular components (*). In comparison, the nucleolus in UTP4 knockdown cells (middle panel) maintained the typical three structural components, fibrillar center (arrow), dense fibrillar components (arrowhead), and granular components (*) as those in the siControl or untreated cells (right panels). (B) Correspondingly, siRPA194 treated, but not siUTP4 treated or control cells, showed segregated caps like localization of UBF as detected at the immunofluorescence microscope level. (C) Quantification showed that the segregation of nucleoli occurs mostly in RPA194 knockdown HeLa cells (n>100 cells, p<0.005 between siRPA194 and all other conditions). Bars =5 mm.

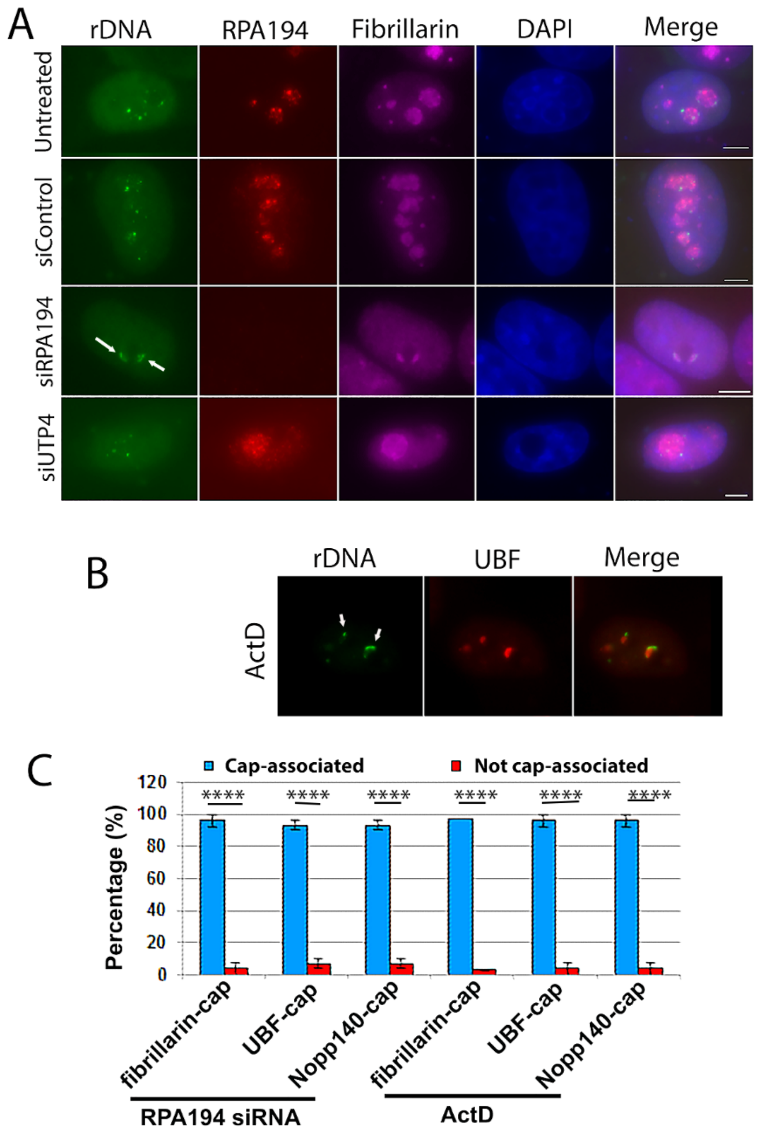

Figure 3: rDNA co-segregated with the fibrillar proteins (fibrillarin or UBF) present in cap structures in segregated nucleoli. (A) Eleven sets of CRISPR-Cas9 sgRNA specifically complementing the rDNA were labeled with MS2-GFP, showing the localization of the rDNA chromatin, which redistributed with the fibrillar components to the nucleolar caps in siRPA194 treated HeLa cells (arrows) similarly to (B) those treated by ActD (arrows). (C) Quantitative evaluation indicated the co-partitioning of rDNA chromatin with the fibrillar components in nearly all of cells treated by siRPA194 or ActD (n>100 cells). Bars = 5 μm

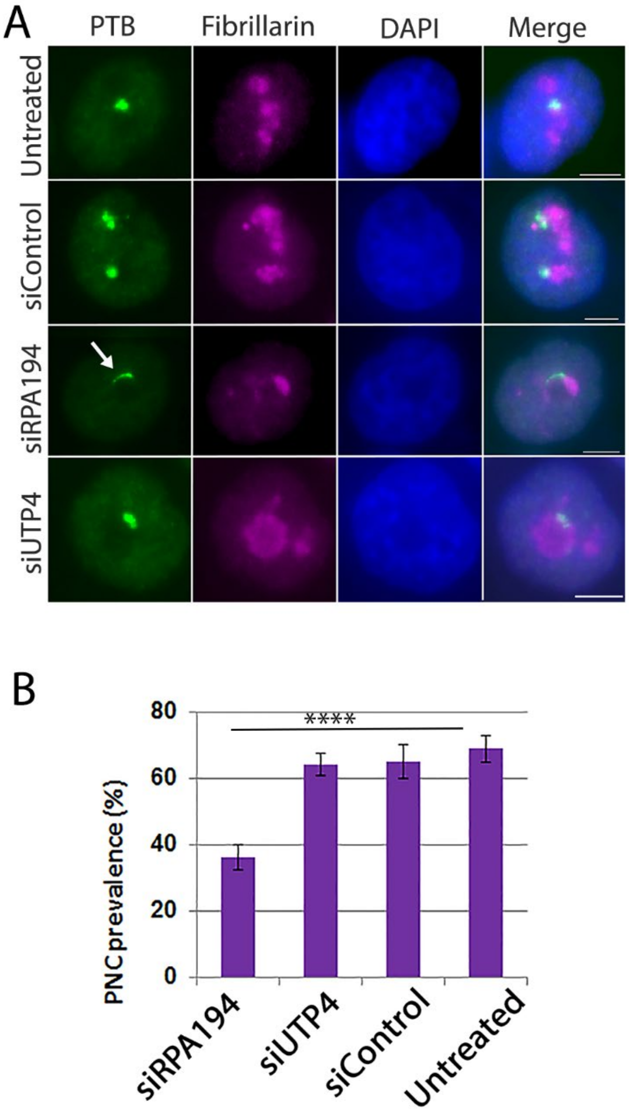

Figure 4: PNC structure and prevalence were altered in siRPA194, but not in siUTP4 treated HeLa cells. (A) The shape of most PNCs was changed, becoming extended (arrows) in siRPA194 treated, but not in siUTP4 treated or control cells. (B) Quantitative analyses demonstrated a significant reduction of PNC prevalence in siRPA194 treated cells (n>100 cells). Bars = 5 µm ****$p<0.001$

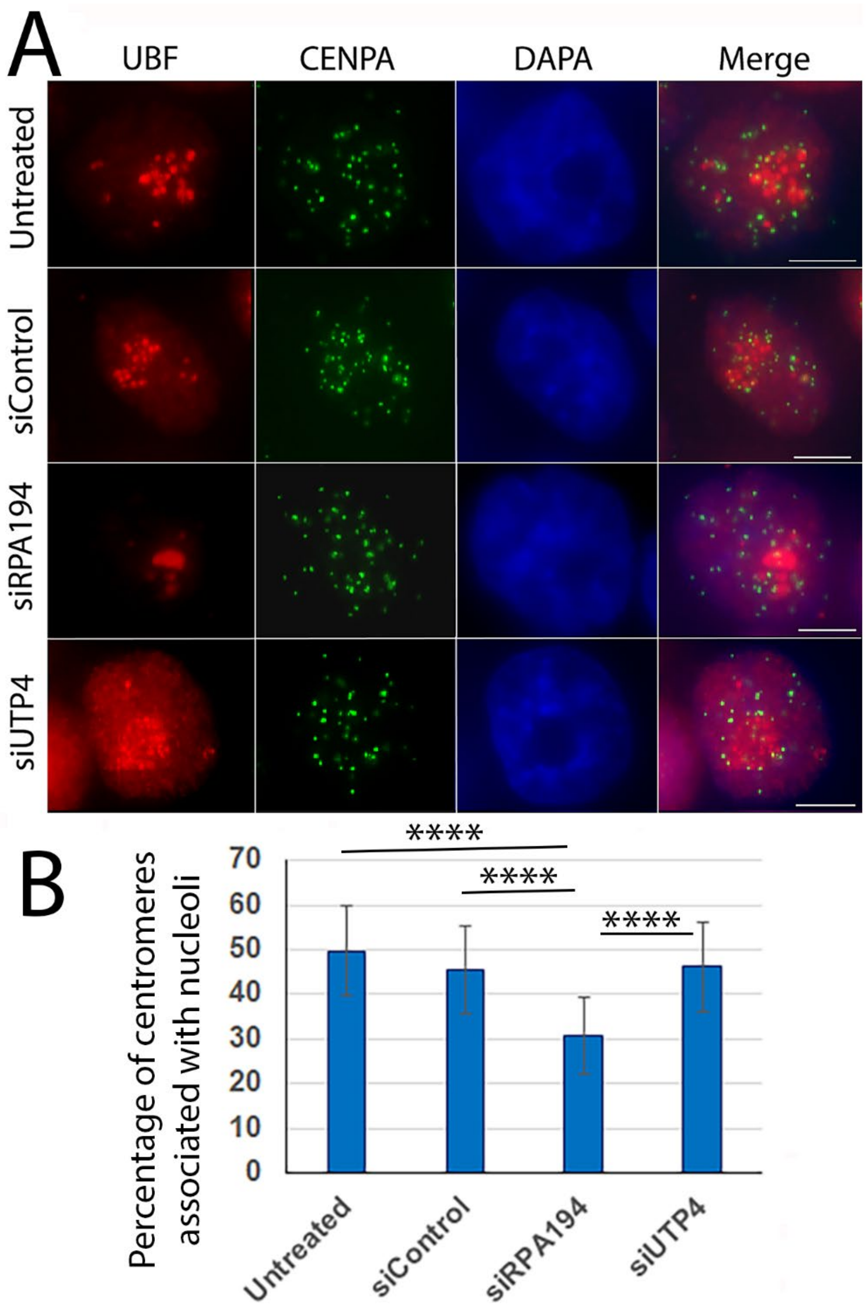

Figure 5: RPA194 knockdown changed nucleoli-centromere interactions (A) The clustering of centromeres (green) around nucleoli (red) decreased in siRPA194 treated, but not in siUTP4 treated and control cells. (B) Quantifying analyses showed changes were statistically significant (n>50 cells) ****p<0,001. Bars = 5 µm

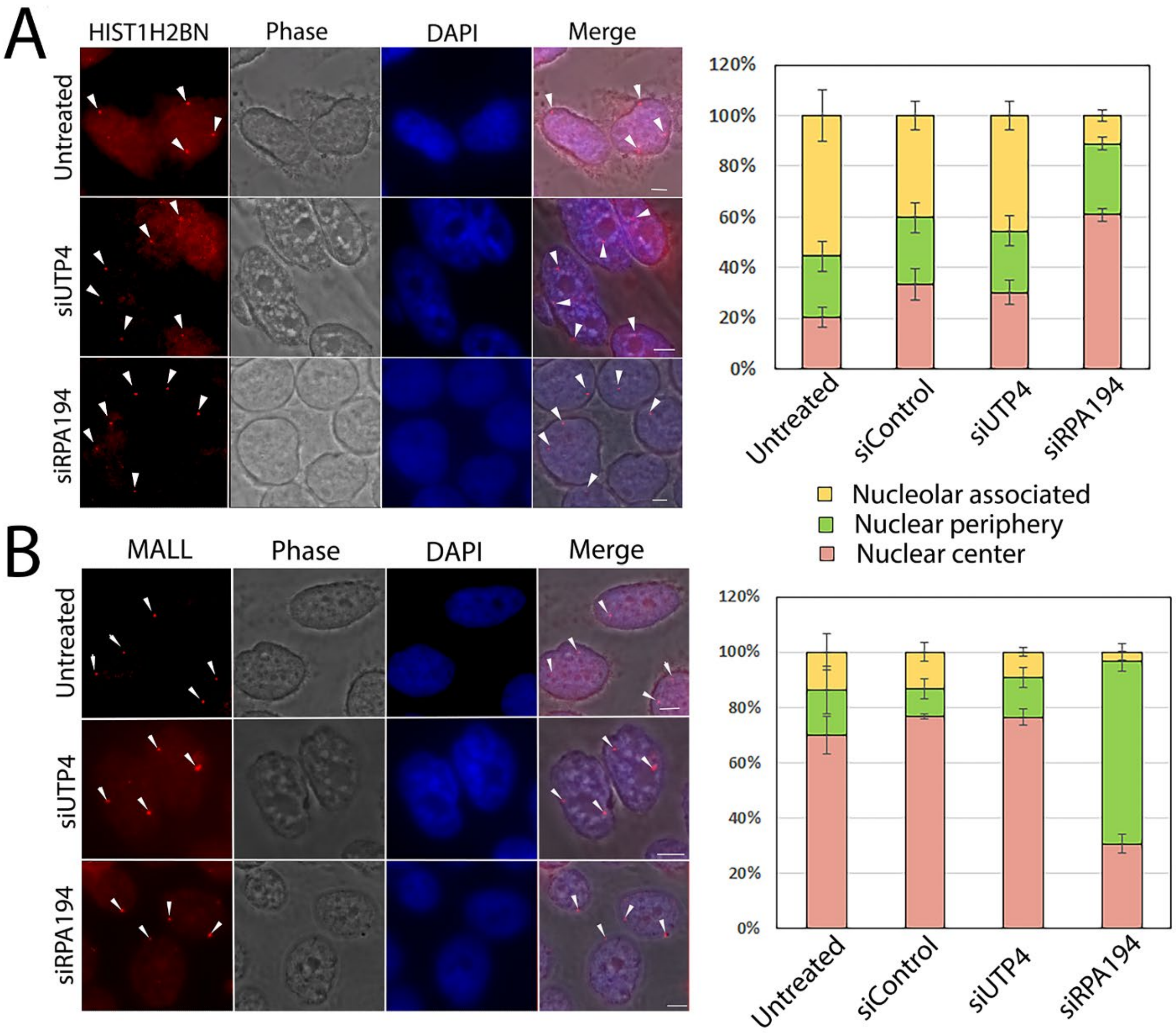

Figure 6: RPA194 knockdown changed spatial distributions of some genes. (A) HIST1H2BN gene loci became more centrally localized in siRPA194 treated HeLa cell nuclei than siUTP4 treated and other control cells (arrowheads) whereas (B) MALL loci became more nuclear peripherally localized in siRPA194 treated cells (arrowheads). Corresponding quantitative analyses showed significant differences in central and peripheral localization of the gene loci between treated and control cells. (n>50 cells) $p<0.01$. Bars = 5 mm

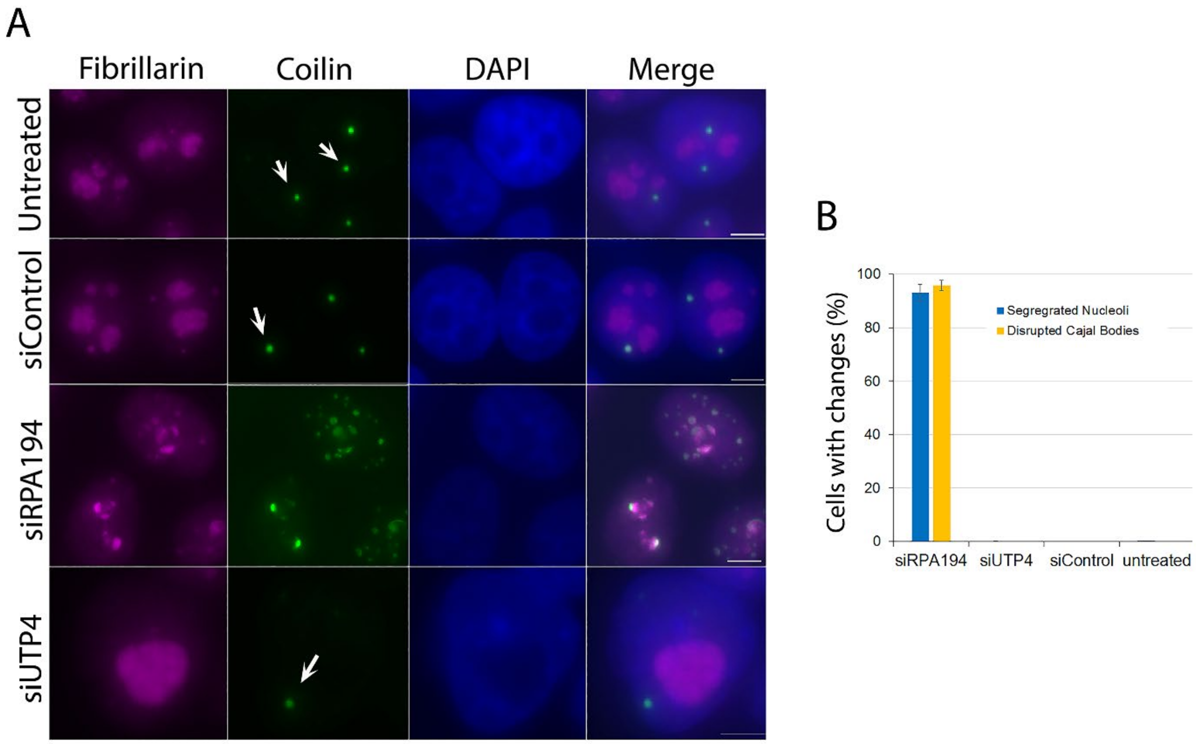

Figure 7: siRPA194, but not siUTP4 treatment, induced disruption of Cajal bodies (arrows). (A) Upon siRPA194 treatment, Cajal bodies became irregularly shaped and some juxtaposed segregated nucleoli in siRPA194 treated cells (third panels), as detected using anti-coilin antibodies. However, Cajal bodies remained round-punctuated spots (arrows) in siUTP4 or control treated cells. (B) Quantitative evaluation showed a close coupling between nucleolar segregation and disruption of Cajal bodies (n>100 cells) (p<0.001 between siRPA194 and all others).

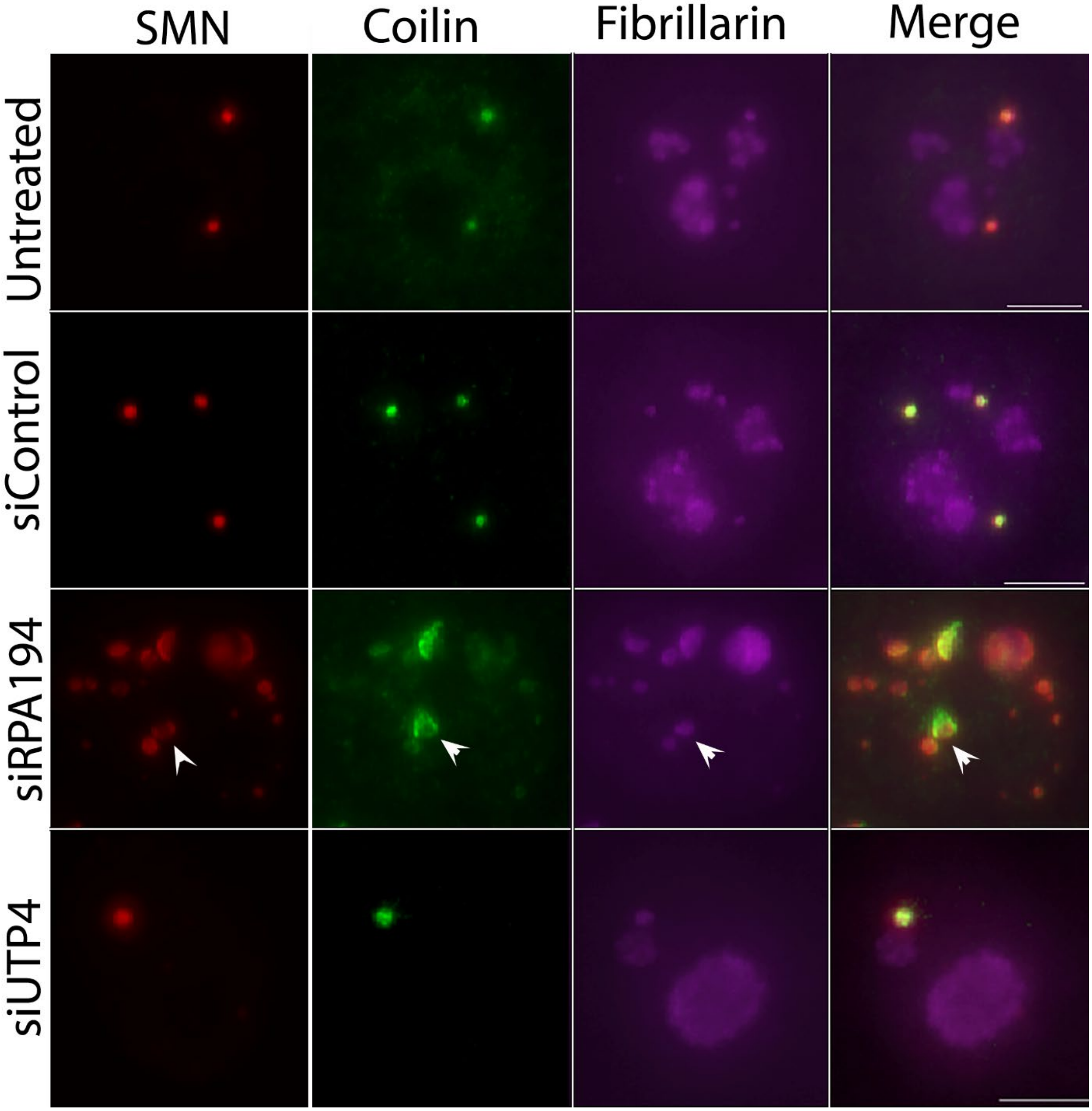

Figure 8: Cajal body components no longer showed nearly complete colocalization in cells with segregated nucleoli from the treatment of siRPA194. Each panel shows a single nucleus. SMN and coilin which normally colocalize to the dotted-like Cajal body structures (Merge) no longer perfectly coincide in the round spots, rather become less colocalized in siRPA194 treated cells (arrowhead). Bar= 5µm

Supplemental material:

Suppl. Table 1: * The exonic and intronic regions of the human reference genome hgp38 were searched with a criterion set at a GC content of between 65 and 100%, as detailed in Materials and Methods. NA: not annotated.

Table S1. Human reference genome sites 65-100% GC*

ID	GC content	Symbol	Gene name
100422838	0.92857143	MIR3195	microRNA 3195
100616250	0.87912088	MIR3960	microRNA 3960
100313781	0.86842105	MIR718	microRNA 718
100616436	0.86363636	MIR4449	microRNA 4449
100616154	0.85185185	MIR4466	microRNA 4466
101929080	0.85106383	LINC02292	long intergenic non-protein coding RNA 2292
102464817	0.83636364	MIR5787	microRNA 5787
100616301	0.82758621	MIR4674	microRNA 4674
100616467	0.82051282	MIR4767	microRNA 4767
100616364	0.80821918	MIR4785	microRNA 4785
102724890	0.80	LINC02293	long intergenic non-protein coding RNA 2293
100616138	0.79761905	MIR4787	microRNA 4787
100616202	0.7962963	MIR4634	microRNA 4634
693157	0.78947368	MIR572	microRNA 572
102465978	0.78688525	MIR6850	microRNA 6850
102465503	0.77777778	MIR6836	microRNA 6836
100422962	0.77419355	MIR4281	microRNA 4281
102464833	0.77272727	MIR6084	microRNA 6084
100616288	0.7721519	MIR4665	microRNA 4665
100616143	0.77173913	MIR4763	microRNA 4763
100287284	0.77142857	MANSC4	MANSC domain containing 4
3222	0.77142857	HOXC5	homeobox C5
8408	0.77142857	ULK1	unc-51 like autophagy activating kinase 1
100616270	0.76712329	MIR4651	microRNA 4651
693149	0.76595745	MIR564	microRNA 564
100302196	0.7625	MIR1234	microRNA 1234
102465493	0.75675676	MIR6821	microRNA 6821
102465431	0.75641026	MIR6722	microRNA 6722
102464835	0.75510204	NA	NA
102466982	0.75384615	MIR6729	microRNA 6729
693235	0.75229358	MIR92B	microRNA 92b
198437	0.75204082	LKAAEAR1	LKAAEAR motif containing 1
100423014	0.75	MIR3196	microRNA 3196
102465836	0.75	MIR7846	microRNA 7846
100616340	0.74647887	MIR4758	microRNA 4758
102465802	0.74576271	MIR7704	microRNA 7704
100126351	0.74390244	MIR939	microRNA 939
100616187	0.74390244	MIR4783	microRNA 4783

57801	0.74318745	HES4	hes family bHLH transcription factor 4
494324	0.74107143	MIR375	microRNA 375
128408	0.73850316	BHLHE23	basic helix-loop-helix family member e23
101926933	0.7384077	LOC101926933	uncharacterized LOC101926933
474383	0.73835125	F8A2	coagulation factor VIII associated 2
163732	0.73480243	CITED4	Cbp/p300 interacting transactivator with Glu/Asp rich carboxy-terminal domain 4
92304	0.73157163	SCGB3A1	secretoglobin family 3A member 1
102465517	0.73134328	MIR6858	microRNA 6858
100616448	0.7297293	NA	NA
442907	0.72972973	MIR339	microRNA 339
100500811	0.72941176	MIR3621	microRNA 3621
2848	0.72744015	GPR25	G protein-coupled receptor 25
102465835	0.72727273	MIR7845	microRNA 7845
389813	0.7266925	AJM1	apical junction component 1 homolog
100423023	0.7260274	MIR3197	microRNA 3197
102465524	0.72580645	MIR6869	microRNA 6869
64975	0.72439204	MRPL41	mitochondrial ribosomal protein L41
102465435	0.72307692	MIR6727	microRNA 6727
100616115	0.72151899	MIR4469	microRNA 4469
100616342	0.72058824	MIR4638	microRNA 4638
5020	0.71937639	OXT	oxytocin/neurophysin I prepropeptide
406941	0.71910112	MIR149	microRNA 149
8511	0.71856608	MMP23A	matrix metallopeptidase 23A (pseudogene)
102464823	0.71666667	MIR6068	microRNA 6068
122748	0.71641791	OR11H6	olfactory receptor family 11 subfamily H member 6
10419	0.71604938	PRMT5	protein arginine methyltransferase 5
101929634	0.71428571	LINC02280	long intergenic non-protein coding RNA 2280
101927953	0.71405094	C5orf66-AS1	C5orf66 antisense RNA 1
345456	0.71320755	PFN3	profilin 3
389199	0.71296296	LOC389199	uncharacterized LOC389199
100302137	0.7125	MIR1914	microRNA 1914
440836	0.71229537	ODF3B	outer dense fiber of sperm tails 3B
100302138	0.71212121	MIR1292	microRNA 1292
102466199	0.71212121	MIR6825	microRNA 6825
100616242	0.71186441	MIR4673	microRNA 4673
79144	0.71072151	PPDPF	pancreatic progenitor cell differentiation and proliferation factor
724028	0.71	MIR658	microRNA 658
100500808	0.70967742	MIR3917	microRNA 3917
100500810	0.70886076	MIR3620	microRNA 3620
100506681	0.70731707	JARID2-AS1	JARID2 antisense RNA 1
54345	0.70679612	SOX18	SRY-box 18
2928	0.70667447	GSC2	goosecoid homeobox 2
100616465	0.70666667	MIR4656	microRNA 4656
643965	0.7060241	TMEM88B	transmembrane protein 88B

100187716	0.70588235	MIR1224	microRNA 1224
168620	0.70538244	BHLHA15	basic helix-loop-helix family member a15
100422893	0.70535714	MIR3154	microRNA 3154
100616438	0.70491803	MIR4632	microRNA 4632
102465434	0.70491803	MIR6726	microRNA 6726
102465491	0.70491803	MIR6819	microRNA 6819
4857	0.70442992	NOVA1	NOVA alternative splicing regulator 1
100313824	0.70434783	MIR663B	microRNA 663b
100616480	0.70422535	MIR4479	microRNA 4479
7293	0.70387487	TNFRSF4	TNF receptor superfamily member 4
94234	0.703207	FOXQ1	forkhead box Q1
643988	0.70311751	FNDC10	fibronectin type III domain containing 10
100616120	0.7027027	MIR4695	microRNA 4695
100847072	0.70212766	MIR5008	microRNA 5008
55194	0.7019774	EVA1B	eva-1 homolog B
100422860	0.70149254	MIR4292	microRNA 4292
55502	0.70075125	HES6	hes family bHLH transcription factor 6
1052	0.70018365	CEBPD	CCAAT enhancer binding protein delta
100126339	0.6996904	MIR941-2	microRNA 941-2
100313887	0.69892473	MIR2277	microRNA 2277
140701	0.69885983	ABHD16B	abhydrolase domain containing 16B
100422889	0.69863014	MIR3194	microRNA 3194
724031	0.69662921	MIR661	microRNA 661
152	0.69516205	ADRA2C	adrenoceptor alpha 2C
415116	0.69506726	PIM3	Pim-3 proto-oncogene, serine/threonine kinase
102466740	0.69491525	MIR6808	microRNA 6808
56731	0.69465021	SLC2A4RG	SLC2A4 regulator
442425	0.69438029	FOXB2	forkhead box B2
345630	0.69387755	FBLL1	fibrillarin like 1
693187	0.69387755	MIR602	microRNA 602
102465526	0.69354839	MIR6872	microRNA 6872
388581	0.69347674	C1QTNF12	C1q and TNF related 12
401115	0.69211325	C4orf48	chromosome 4 open reading frame 48
1365	0.69152276	CLDN3	claudin 3
100126329	0.69021739	MIR941-1	microRNA 941-1
100847037	0.69	MIR5001	microRNA 5001
54729	0.69	NKX1-1	NK1 homeobox 1
54461	0.68958236	FBXW5	F-box and WD repeat domain containing 5
100616160	0.68918919	MIR4655	microRNA 4655
100422950	0.68852459	MIR3141	microRNA 3141
102466223	0.68852459	MIR7114	microRNA 7114
388849	0.68776052	CCDC188	coiled-coil domain containing 188
100616346	0.6875	MIR4649	microRNA 4649
9022	0.68741355	CLIC3	chloride intracellular channel 3
29952	0.68701467	DPP7	dipeptidyl peptidase 7
7349	0.68642447	UCN	urocortin

2875	0.68443598	GPT	glutamic--pyruvic transaminase
8326	0.68434559	FZD9	frizzled class receptor 9
389816	0.68422684	LRRC26	leucine rich repeat containing 26
102464824	0.6835443	MIR6069	microRNA 6069
94032	0.68280764	CAMK2N2	calcium/calmodulin dependent protein kinase II inhibitor 2
7425	0.68265802	VGF	VGF nerve growth factor inducible
2301	0.68248359	FOXE3	forkhead box E3
102465490	0.68181818	MIR6816	microRNA 6816
100423020	0.68131868	MIR4258	microRNA 4258
102466271	0.68115942	MIR6893	microRNA 6893
8971	0.68044417	H1FX	H1 histone family member X
729627	0.6803995	PRR23A	proline rich 23A
101927062	0.68037135	LINC02294	long intergenic non-protein coding RNA 2294
4582	0.68010715	MUC1	mucin 1, cell surface associated
551	0.67957584	AVP	arginine vasopressin
163933	0.67923795	FAM43B	family with sequence similarity 43 member B
414919	0.67882353	C8orf82	chromosome 8 open reading frame 82
339451	0.6786898	KLHL17	kelch like family member 17
728229	0.67821068	TMEM191B	transmembrane protein 191B
100169751	0.6781923	RNA5S1	RNA, 5S ribosomal 1
84808	0.67764877	PERM1	PPARGC1 and ESRR induced regulator, muscle 1
100422927	0.67692308	MIR4291	microRNA 4291
54863	0.67688535	TOR4A	torsin family 4 member A
100316904	0.67671061	SAP25	Sin3A associated protein 25
83590	0.67612485	TMUB1	transmembrane and ubiquitin like domain containing 1
165257	0.67585946	C1QL2	complement C1q like 2
92070	0.67567568	CTBP1-DT	CTBP1 divergent transcript
150223	0.67560729	YDJC	YdjC chitooligosaccharide deacetylase homolog
10227	0.67550593	MFSD10	major facilitator superfamily domain containing 10
6576	0.67536855	SLC25A1	solute carrier family 25 member 1
402635	0.67528035	GRIFIN	galectin-related inter-fiber protein
353137	0.67507003	LCE1F	late cornified envelope 1F
8784	0.67462312	TNFRSF18	TNF receptor superfamily member 18
339456	0.67458432	TMEM52	transmembrane protein 52
377841	0.67435932	ENTPD8	ectonucleoside triphosphate diphosphohydrolase 8
3083	0.67433303	HGFAC	HGF activator
83481	0.6742822	EPPK1	epiplakin 1
653604	0.67396594	HIST2H3D	histone cluster 2 H3 family member d
51162	0.6730811	EGFL7	EGF like domain multiple 7
101928767	0.67307692	LINC02328	long intergenic non-protein coding RNA 2328
116983	0.67297203	ACAP3	ArfGAP with coiled-coil, ankyrin repeat and PH domains 3
441478	0.67288136	NRARP	NOTCH regulated ankyrin repeat protein
100423027	0.67272727	MIR4266	microRNA 4266

340260	0.67225748	UNCX	UNC homeobox
102466748	0.67213115	MIR6845	microRNA 6845
642658	0.67169615	SCX	scleraxis bHLH transcription factor
102465977	0.67164179	MIR6829	microRNA 6829
100526833	0.67152125	SEPT5-GP1BB	SEPT5-GP1BB readthrough
91289	0.67151592	LMF2	lipase maturation factor 2
102465511	0.67142857	MIR6848	microRNA 6848
221908	0.67133956	PPP1R35	protein phosphatase 1 regulatory subunit 35
9997	0.67130919	SCO2	SCO2, cytochrome c oxidase assembly protein
386685	0.67124857	KRTAP10-12	keratin associated protein 10-12
4738	0.67124071	NEDD8	neural precursor cell expressed, developmentally down-regulated 8
647219	0.67112676	ASCL5	achaete-scute family bHLH transcription factor 5
4056	0.67091454	LTC4S	leukotriene C4 synthase
100423011	0.67073171	MIR3138	microRNA 3138
440829	0.67031678	SHISA8	shisa family member 8
100126332	0.67021277	MIR943	microRNA 943
3754	0.67016164	KCNF1	potassium voltage-gated channel modifier subfamily F member 1
389332	0.67006599	SMIM32	small integral membrane protein 32
113655	0.66962617	MFSD3	major facilitator superfamily domain containing 3
54998	0.66874292	AURKAIP1	aurora kinase A interacting protein 1
727800	0.66852368	RNF208	ring finger protein 208
142680	0.66850638	SLC34A3	solute carrier family 34 member 3
25907	0.66850524	TMEM158	transmembrane protein 158 (gene/pseudogene)
102724312	0.66840149	LINC01770	long intergenic non-protein coding RNA 1770
54905	0.66811549	CYP2W1	cytochrome P450 family 2 subfamily W member 1
30012	0.66783585	TLX3	T cell leukemia homeobox 3
83482	0.66783278	SCRT1	scratch family transcriptional repressor 1
402682	0.66767068	UFSP1	UFM1 specific peptidase 1 (inactive)
126789	0.66763099	PUSL1	pseudouridylate synthase-like 1
23237	0.66754156	ARC	activity regulated cytoskeleton associated protein
83756	0.66741798	TAS1R3	taste 1 receptor member 3
53834	0.66729712	FGFRL1	fibroblast growth factor receptor like 1
7012	0.66728281	TERC	telomerase RNA component
2907	0.66676593	GRINA	glutamate ionotropic receptor NMDA type subunit associated protein 1
100302156	0.66666667	MIR1229	microRNA 1229
100302237	0.66666667	MIR1281	microRNA 1281
100422939	0.66666667	MIR3147	microRNA 3147
100616178	0.66666667	MIR4641	microRNA 4641
100616353	0.66666667	NA	NA
100616367	0.66666667	MIR4467	microRNA 4467
102465438	0.66666667	MIR6732	microRNA 6732
693232	0.66666667	MIR647	microRNA 647
20	0.66662058	ABCA2	ATP binding cassette subfamily A member 2

386676	0.66609735	KRTAP10-9	keratin associated protein 10-9
407003	0.66555851	MIR219A2	microRNA 219a-2
441869	0.66507463	ANKRD65	ankyrin repeat domain 65
170487	0.66469428	ACTL10	actin like 10
11219	0.66459276	TREX2	three prime repair exonuclease 2
26233	0.66447035	FBXL6	F-box and leucine rich repeat protein 6
389058	0.66422287	SP5	Sp5 transcription factor
100288152	0.66419919	SLC9A3-AS1	SLC9A3 antisense RNA 1
84968	0.66417028	PNMA6A	PNMA family member 6A
102577424	0.66416792	LINC01574	long intergenic non-protein coding RNA 1574
142678	0.66405633	MIB2	mindbomb E3 ubiquitin protein ligase 2
347454	0.66365979	SOWAHD	sosondowah ankyrin repeat domain family member D
6754	0.66362999	SSTR4	somatostatin receptor 4
64856	0.66355024	VWA1	von Willebrand factor A domain containing 1
386677	0.66337449	KRTAP10-1	keratin associated protein 10-1
100191040	0.6630157	C2CD4D	C2 calcium dependent domain containing 4D
158056	0.66277772	MAMDC4	MAM domain containing 4
100302259	0.6626506	MIR1202	microRNA 1202
1855	0.66245115	DVL1	dishevelled segment polarity protein 1
10912	0.66234608	GADD45G	growth arrest and DNA damage inducible gamma
100126350	0.66233766	MIR933	microRNA 933
29085	0.66232639	PHPT1	phosphohistidine phosphatase 1
386679	0.66231506	KRTAP10-2	keratin associated protein 10-2
100500835	0.66225166	MIR3907	microRNA 3907
1059	0.66197183	CENPB	centromere protein B
1051	0.66155419	CEBPB	CCAAT enhancer binding protein beta
100500913	0.66153846	MIR3714	microRNA 3714
102465507	0.66153846	MIR6842	microRNA 6842
8941	0.66148325	CDK5R2	cyclin dependent kinase 5 regulatory subunit 2
56033	0.66142362	BARX1	BARX homeobox 1
8484	0.66130558	GALR3	galanin receptor 3
5365	0.66127648	PLXNB3	plexin B3
646960	0.66121051	PRSS56	serine protease 56
11255	0.6611929	HRH3	histamine receptor H3
85441	0.66076514	HELZ2	helicase with zinc finger 2
26086	0.6605042	GPSM1	G protein signaling modulator 1
339983	0.66036751	NAT8L	N-acetyltransferase 8 like
339453	0.66022727	TMEM240	transmembrane protein 240
100419743	0.66012489	DBET	D4Z4 binding element transcript (non-protein coding)
389333	0.66009371	PROB1	proline rich basic protein 1
148398	0.659933	SAMD11	sterile alpha motif domain containing 11
79581	0.6597086	SLC52A2	solute carrier family 52 member 2
390992	0.65969719	HES3	hes family bHLH transcription factor 3
441476	0.65946919	STPG3	sperm-tail PG-rich repeat containing 3

100422826	0.65934066	MIR4274	microRNA 4274
6339	0.65930654	SCNN1D	sodium channel epithelial 1 delta subunit
26873	0.65926633	OPLAH	5-oxoprolinase, ATP-hydrolysing
101928158	0.65920826	LAMA5-AS1	LAMA5 antisense RNA 1
643596	0.65920608	RNF224	ring finger protein 224
386680	0.65913043	KRTAP10-5	keratin associated protein 10-5
2783	0.65910702	GNB2	G protein subunit beta 2
8636	0.65893271	SSNA1	SS nuclear autoantigen 1
5413	0.65887534	5-Sep	septin 5
80139	0.65886209	ZNF703	zinc finger protein 703
386681	0.6586758	KRTAP10-8	keratin associated protein 10-8
56654	0.65859816	NPDC1	neural proliferation, differentiation and control 1
100422994	0.65853659	MIR4267	microRNA 4267
644524	0.65852742	NKX2-4	NK2 homeobox 4
2261	0.65822947	FGFR3	fibroblast growth factor receptor 3
677766	0.65807963	SCARNA2	small Cajal body-specific RNA 2
100130449	0.65794162	LOC100130449	uncharacterized LOC100130449
100423028	0.65789474	MIR4254	microRNA 4254
391723	0.65784114	HELT	helt bHLH transcription factor
100422928	0.65765766	MIR3127	microRNA 3127
100126348	0.65740741	MIR760	microRNA 760
401357	0.65740741	LOC401357	uncharacterized LOC401357
954	0.65736382	ENTPD2	ectonucleoside triphosphate diphosphohydrolase 2
118442	0.65723414	GPR62	G protein-coupled receptor 62
375790	0.65710079	AGRN	agrin
158062	0.65628761	LCN6	lipocalin 6
693159	0.65625	MIR574	microRNA 574
8022	0.65586907	LHX3	LIM homeobox 3
102465536	0.6557377	MIR6890	microRNA 6890
4636	0.65542938	MYL5	myosin light chain 5
389458	0.65514104	RBAKDN	RBAK downstream neighbor (non-protein coding)
9401	0.65507777	RECQL4	RecQ like helicase 4
3425	0.65448315	IDUA	iduronidase, alpha-L-
102060282	0.65443038	RASSF1-AS1	RASSF1 antisense RNA 1
401934	0.65439856	RNF223	ring finger protein 223
100616447	0.65432099	MIR4780	microRNA 4780
255374	0.65429363	MBLAC1	metallo-beta-lactamase domain containing 1
386674	0.6542811	KRTAP10-6	keratin associated protein 10-6
5600	0.65386251	MAPK11	mitogen-activated protein kinase 11
100129722	0.65385788	STPG3-AS1	STPG3 antisense RNA 1
90120	0.65351389	TMEM250	transmembrane protein 250
386684	0.65324385	KRTAP12-4	keratin associated protein 12-4
54587	0.65298713	MXRA8	matrix remodeling associated 8
733	0.6529786	C8G	complement C8 gamma chain
100286938	0.65294592	VPS13A-AS1	VPS13A antisense RNA 1
386682	0.65293512	KRTAP10-3	keratin associated protein 10-3

51052	0.65282392	PRLH	prolactin releasing hormone
80772	0.65258329	CPTP	ceramide-1-phosphate transfer protein
84179	0.65243662	SLC49A3	solute carrier family 49 member 3
26012	0.6521887	NSMF	NMDA receptor synaptonuclear signaling and neuronal migration factor
286256	0.65209349	LCN12	lipocalin 12
100616312	0.65116279	MIR4478	microRNA 4478
5730	0.65111587	PTGDS	prostaglandin D2 synthase
1961	0.6510623	EGR4	early growth response 4
100422975	0.65079365	MIR4252	microRNA 4252
102466270	0.65079365	MIR6741	microRNA 6741
137797	0.65073375	LYPD2	LY6/PLAUR domain containing 2
100500828	0.65060241	MIR3619	microRNA 3619
114822	0.65000651	RHPN1	rhophilin Rho GTPase binding protein 1

* The exonic and intronic regions of the human reference genome hgp38 were searched with a criterion set at a GC content of between 65 and 100%, as detailed in Materials and Methods. NA: not annotated.

s

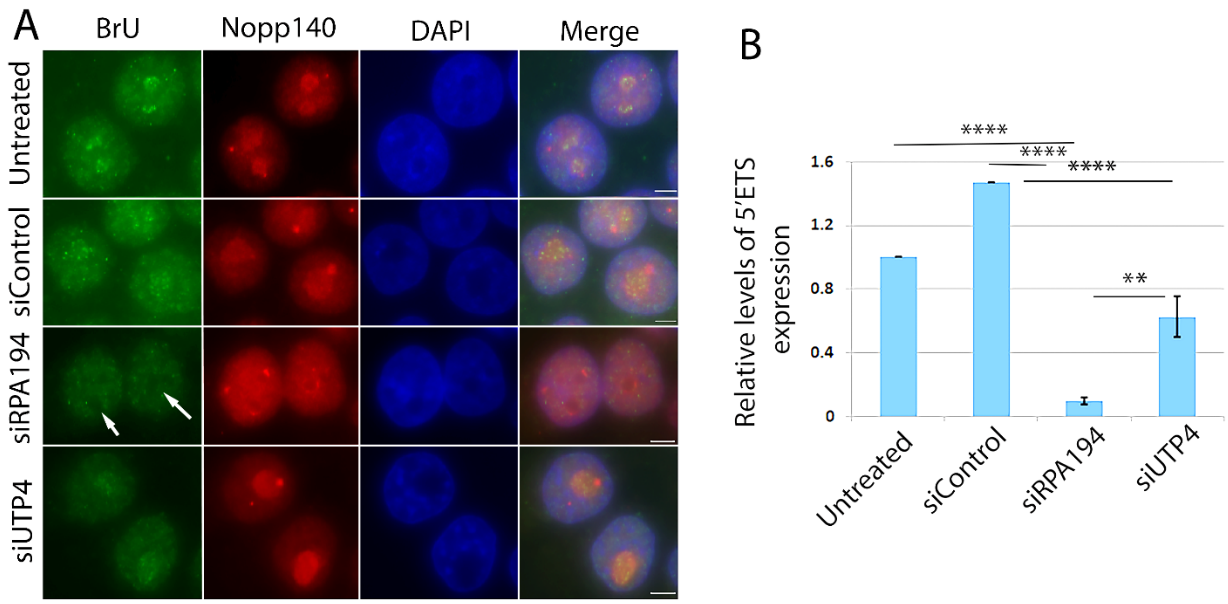

Suppl. Figure 1: The transcription of rDNA was significantly reduced in cells treated with siRPA194 and to a lesser extent with siUTP4. (A) BrU pulse labeling for 5 minutes showed a significant loss of BrU signal in siRPA194 treated cells (A, arrows), compared to controls where more intense labeling was detected in nucleoli. (B) Quantitative RT-PCR showed a significant reduction in 5'ETS RNA expression in siRPA194 and siUTP4 treated cells. Bar= 5 mm. ****p<0.001, **p<0.01

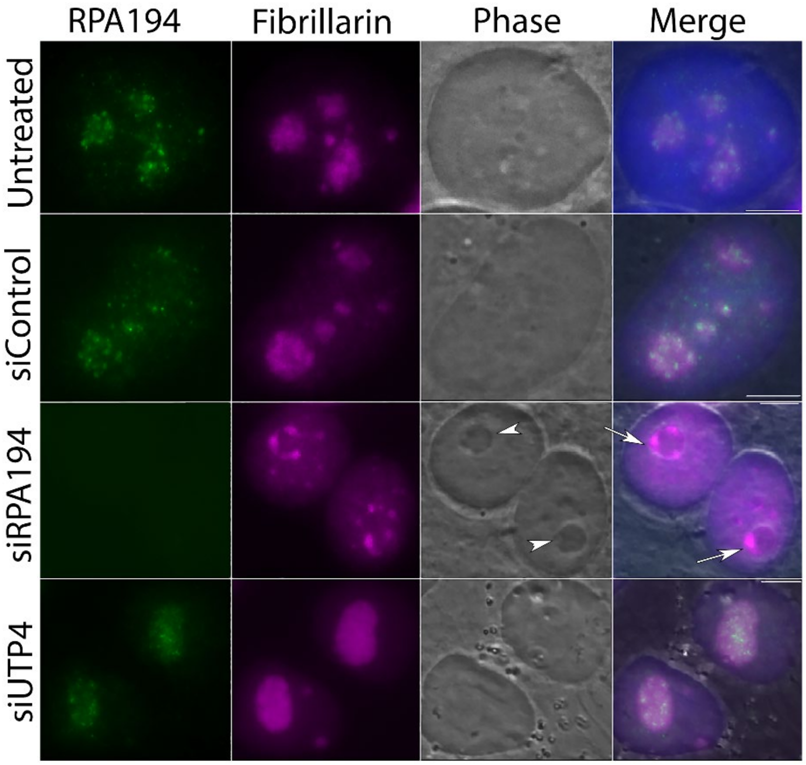

Suppl. Figure 2: siRPA194, but not siUTP4 treated HeLa cells, lost the RPA194 signal (green). Nucleolar segregation was detected by the immunolabeling of fibrillarin (magenta). Cap-like structures enriched with firbrillar components (arrows) juxtaposed the reminants of the nucleoli primarily containing granular components (arrowheads). Bars= 5 mm

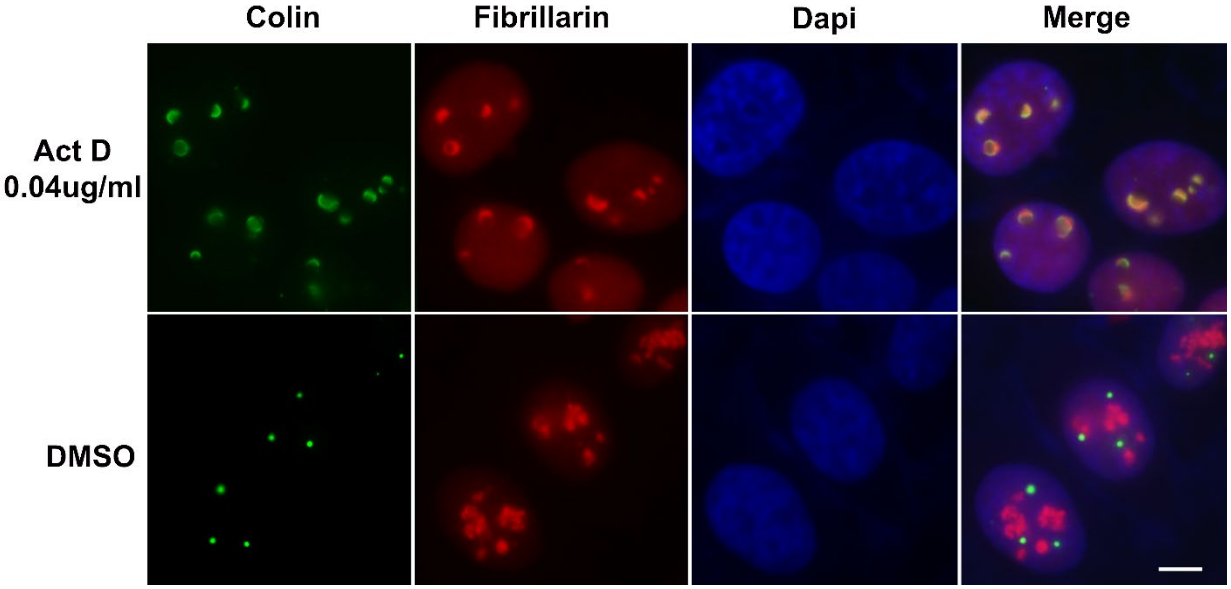

Suppl. Figure 3: Treatment with a low concentration (0.04ug/ml) of actinomycin D (Act D) induces nucleolar segregations and disruption of Cajal bodies as detected by anti-fibrillarin antibodies (red) and anti-coilin (green) antibodies. Bar= 5 mm

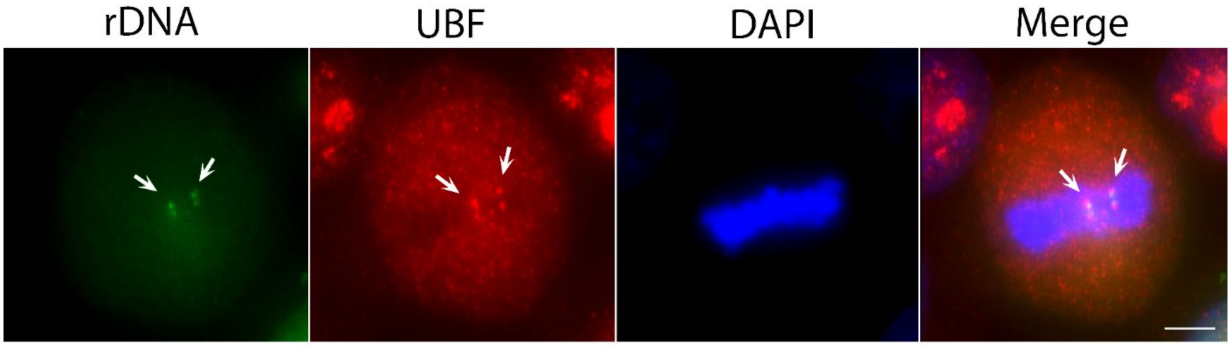

Suppl. Figure 4: The CRISPR-Cas9 sgRNA labeling of rDNA was validated using mitotic cells where UBF was found to be colocalized with the labeling (arrows), confirming that the sgRNA sets indeed labeled rDNA chromatin on mitotic chromosomes (arrow). Bar= 5 mm

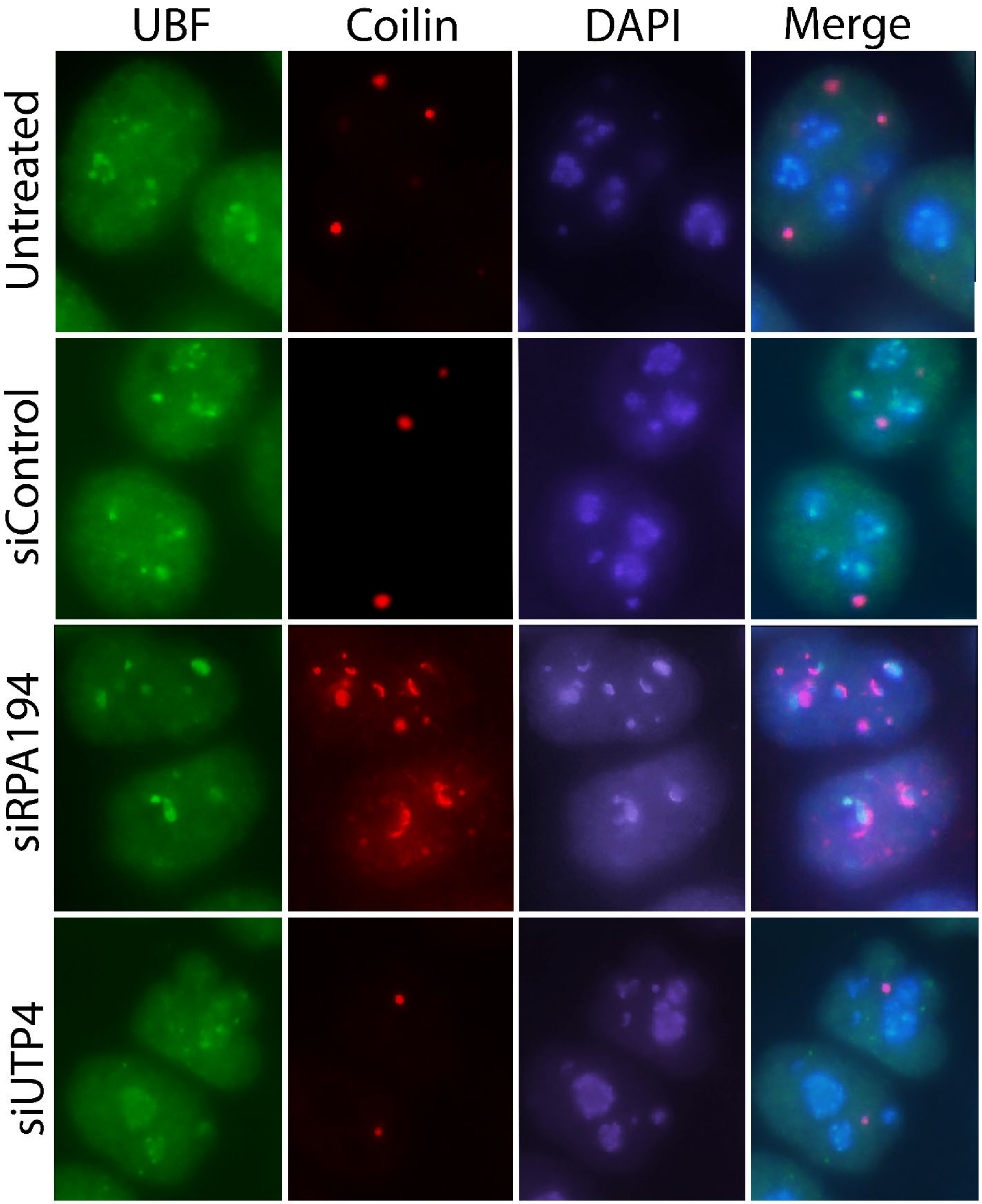

Suppl. Fig. 5: Cajal bodies are significantly altered in siRPA194 treated cells. Cells were co-immunolabeled with antibodies against UBF and coilin. Bar= 5 mm

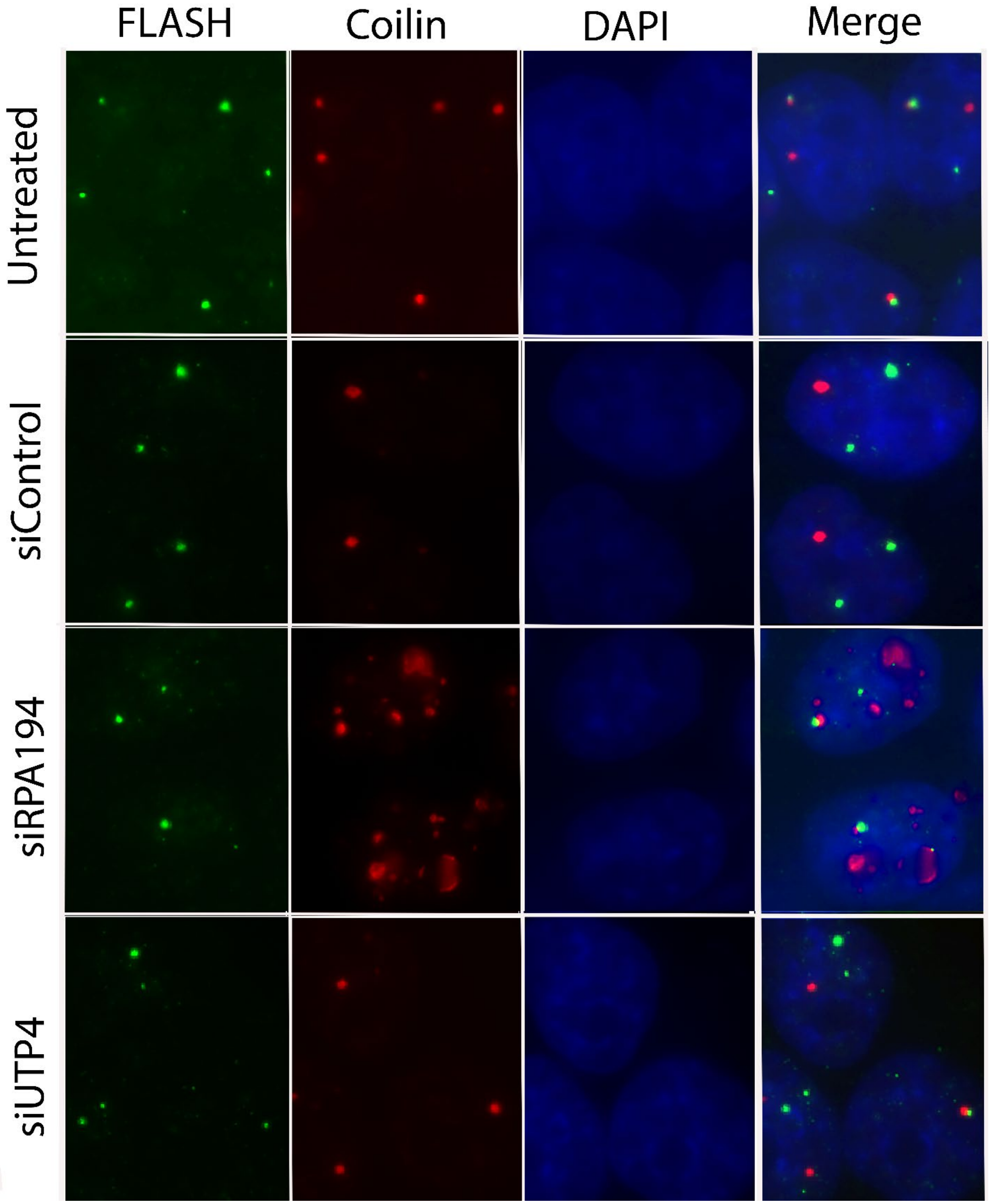

Suppl. Figure 6: While Cajal bodies change significantly in siRPA194 treated cells, histone locus bodies do not show detectable changes. Bar= 5 mm